



저작자표시-비영리-변경금지 2.0 대한민국

이용자는 아래의 조건을 따르는 경우에 한하여 자유롭게

- 이 저작물을 복제, 배포, 전송, 전시, 공연 및 방송할 수 있습니다.

다음과 같은 조건을 따라야 합니다:



저작자표시. 귀하는 원저작자를 표시하여야 합니다.



비영리. 귀하는 이 저작물을 영리 목적으로 이용할 수 없습니다.



변경금지. 귀하는 이 저작물을 개작, 변형 또는 가공할 수 없습니다.

- 귀하는, 이 저작물의 재이용이나 배포의 경우, 이 저작물에 적용된 이용허락조건을 명확하게 나타내어야 합니다.
- 저작권자로부터 별도의 허가를 받으면 이러한 조건들은 적용되지 않습니다.

저작권법에 따른 이용자의 권리는 위의 내용에 의하여 영향을 받지 않습니다.

이것은 [이용허락규약\(Legal Code\)](#)을 이해하기 쉽게 요약한 것입니다.

[Disclaimer](#)

Ph.D. Dissertation of Engineering

Crystal Structure Engineering of Hybrid Perovskites for Efficient Light-Emitting Diodes

결정 구조 변화를 이용한 고효율 페로브스카이트
발광 다이오드 구현

August 2022

Graduate School of Engineering
Seoul National University
Materials Science and Engineering

Jung-Min Heo

Crystal Structure Engineering of Hybrid Perovskites for Efficient Light-Emitting Diodes

Advisor: Tae-Woo Lee

Submitting a Ph.D. Dissertation of Engineering

August 2022

Graduate School of Engineering
Seoul National University
Materials Science and Engineering

Jung-Min Heo

Confirming the Ph.D. Dissertation is written by

Jung-Min Heo

August 2022

Chair 박병우 (Seal)

Vice Chair 이태우 (Seal)

Examiner 김진영 (Seal)

Examiner 이재상 (Seal)

Examiner 조힘찬 (Seal)

Abstract

Metal halide hybrid perovskites have great attention for optoelectronic applications (e.g., solar cells, light-emitting diodes (LEDs), laser, transistor, and memory devices) in a short time. Especially, hybrid perovskites have excellent characteristics for emitters such as i) easy color tuning, ii) good photoluminescence, iii) narrow emission spectrum (small full width half-maximum length), and balanced charge carrier mobility. Based on these advantages, researchers introduce lots of strategies such as additive engineering, anti-solvent methods, structure modification, and dimension control since the first room temperature perovskite light-emitting diodes (PeLEDs) in 2012. However, the development of efficient and large-area PeLEDs is still underdeveloped due to the limitations of crystal structure instability and the limitation of solution processing.

In this thesis, we develop highly efficient and stable PeLEDs by structure modulation. These results are almost the same with conventional commercialized LED devices such as organic LEDs and quantum dot LEDs. The principle approach is the crystal structure engineering using various methods such as additive engineering, A-site cation modification, and introducing longer organic alkyl ammonium for dimension control of perovskite.

In **the first chapter**, a general introduction would be presented. **The second chapter** will be deal with how to improve device efficiency and stability in single cation perovskite by additive engineering. Defect engineering of perovskite and suppression of exciton loss are crucial for device performances. Here, we use 1,8-octanedithiol that is dominantly distributed at the lower part of a methylammonium lead bromide (MAPbBr₃) emitting layer. The dithiol additive can perform a

multifunctional role in defect passivation, spatial confinement of excitons, and prevention of exciton quenching at the interface between the perovskite layer and the underlying hole-injection layer. Photoluminescence studies reveal the enhanced charge carrier dynamics of the perovskite emitters with the use of the thiol additive, which improves perovskite LEDs' efficiency and stability. **In the third chapter**, I introduce the quadruple cation perovskite structure for defect passivation of 3D polycrystalline perovskite. Recently, several papers have been reported about PeLEDs that have highly efficient characteristics, but these have not been realized high luminance, high efficiency and long lifetime at the same time. Polycrystalline 3D perovskites have excellent charge transport properties intrinsically. However, they are not favorable for achieving high luminous efficiency due to weak carrier confinement and high defect density. On the other hand, colloidal perovskite nanocrystals have strong carrier confinement and low defect density, but also they are suffers from poor charge transport because of insulating ligands, resulting in low brightness and poor operation lifetime. Here, we report a defect-free quadruple perovskite by Guanidium (GA) cooperation into A-site cation in crystal structure. We demonstrate efficient, bright, and stable green PeLEDs that have maximum brightness of $\sim 470,000 \text{ cd m}^{-2}$, maximum current efficiency of 150 cd A^{-1} (external quantum efficiency of 28.94%), and very long estimated half-lifetime of $>14\text{h}$ at $100,00 \text{ cd m}^{-2}$. We show that quadruple cation system can effectively passivate the high defect nature of polycrystalline 3D perovskite, and thereby realize strong charge confinement and greatly reduced trap density while maintaining the good charge transport properties of 3D perovskites. **In the fourth chapter**, vapor-deposition method is introduced. In these days, most of researcher have focused on the solution-processed perovskite optoelectronics because of easy-fabrication characteristics.

However, vapor-deposition methods are needed for the commercializing of perovskite as an emitter. Therefore, we introduce the physical vapor methods for PeLEDs. Especially, we could make CsPbBr₃ films with single-source vapor-deposition methods by making CsPbBr₃ powder for the single-source vapor-deposition, and then we control the chemical stoichiometric ratio for the efficient luminance characteristics. Moreover, quasi-2D structure are firstly introduced for the vapor-deposited PeLEDs. we could see the energy funneling effect by structure modification and demonstrate the bright (>1,000 cd m⁻²) PeLEDs. This works shows the possibility of structure modification of perovskite with vapor-deposition methods. Lastly, the present thesis is summarized, and a conclusion is drawn in **the fifth chapter**. With the presented findings, a better understanding of the perovskite structure modulation, and could be the cornerstone of commercialization of PeLEDs.

Keyword: Perovskite light-emitting diodes, Sulfur additive, A-site cation substitution, Guanidium, Vapor-deposition, Quasi-2D structure

Student Number: 2019-38576

Table of Contents

Abstract	i
Contents.....	iv
List of Tables	viii
List of Figures	ix
Chapter 1. Introduction	1
1.1 Overview of Perovskites	1
1.2 Demisionality and Structure of Perovskites.....	3
1.3 Vapor-deposition methods.....	5
1.4 Research strategies	7
1.5 Biobliography.....	9
Chapter 2. Multifuncional Dithiol Additive in Polycrystalline Perovskite Emitters for Suppression of Non-Radiative Recombination	13
2.1 Introduction.....	13
2.2 Materials and experiments	17
2.3 Results and discussion	21
2.4 Conclusion	35
2.5 Biobliography.....	38
Chapter 3. Ideal Mixed-Cation System for Highly Efficient and Stable Perovskite Light-Emitting Diodes.....	46
3.1 Introduction.....	46
3.2 Materials and experiments	51

3.3 Results and discussion	55
3.4 Conclusion	63
3.5 Bibliography.....	65
Chapter 4. High-efficiency Quasi-2D Perovskite Light-Emitting Diodes using Vapor-deposition methods	68
4.1 Introduction.....	68
4.2 Materials and experiments	70
4.3 Results and discussion	74
4.4 Conclusion	84
4.5 Bibliography.....	85
Chapter 5. Summary	89
Abstract in Korean	90

List of Tables

Table 2-1. Summary of the reported PeLEDs using MAPbBr ₃ emitter.....	36
Table 2-2. Bi-exponential decay function fitted results of PL lifetime curves of pristine and thiol-incorporated MAPbBr ₃ films on glass/CPA substrates.....	36
Table 2-3. Device characteristics of PeLEDs using pristine or thiol-incorporated MAPbBr ₃ based on different anode.....	37
Table 3-1. Table of CE, EQE, Luminance PeLEDs characteristics with different GA ratio.....	63
Table 3-2. single-carrier device results for the trap density calculation both w/ GA cation and w/o GA.....	64
Table 3-3. Table of CE, EQE, Luminance PeLEDs characteristics with different mixed cation system.	64

List of Figures

Figure 1-1. a) Structure properties b) Fundamental limitation as an emitter c) Emergence of future emitter with perovskite materials.....	2
Figure 1-2. Illustration of benefit of low-dimensional Structure perovskite	4
Figure 1-3. The difference between solution-processing and thermal deposition..	5
Figure 1-4. Illustration of research overview	8
Figure 2-1. Schematic illustrations of (a) Lewis-base passivation of undercoordinated Pb^{2+} by ODT, (b) spatial confinement of exciton inside grains by ODT, and (c) efficient radiative recombination with the use of ODT that prevents exciton quenching at the interface of perovskite/HIL... ..	15
Figure 2-2. EQE developments of the reported PeLEDs that are used $MAPbBr_3$ as an emitter.. ..	16
Figure 2-3 (a) 1H NMR spectra of $MAPbBr_3$ (black), $MAPbBr_3$ with ODT (10 vol%) (red) in $DMSO-d_6$, and pure ODT (blue). (b) DSIMS depth profile of perovskite films. Distributions of S and Br in PP $MAPbBr_3$ (black) and CSMP $MAPbBr_3$ (red). (c) HAADF scanning STEM cross-section image of thiol-incorporated perovskite film. (d) Integrated EDX spectra of the acquired data from the red boxed areas in (c).. ..	23
Figure 2-4. 1H NMR spectra of pristine $MAPbBr_3$ (black) and $MAPbBr_3$ with ODT (10 vol%) (blue) in $DMSO-d_6$	24
Figure 2-5. 1H NMR spectra of $MAPbBr_3$ with ODT (10 vol%) (blue) and pristine ODT (red) in $DMSO-d_6$ showing signals of proton bonded to carbon within ODT as correspondingly denoted.	24

Figure 2-6. SEM images of pristine MAPbBr ₃ and thiol-incorporated MAPbBr ₃ films and corresponding grain size distribution..	25
Figure 2-7. XRD pattern of pristine MAPbBr ₃ (black) and MAPbBr ₃ with the incorporation of ODT (red)..	25
Figure 2-8. Steady-state PL spectrum of thiol-incorporated MAPbBr ₃ (red) and pristine MAPbBr ₃ (black) excited (a) from the substrate side and (b) from the film side. (c) Transient PL decay curves of the films..	27
Figure 2-9. (a) Temperature-dependent integrated PL intensity of pristine and thiol-incorporated MAPbBr ₃ films. Solid lines are fits to the data using the Arrhenius equation. Excitation-power dependent normalized PL intensity at (b) 80 K and (c) 300 K. Solid lines are linear fits to the data with a power-law k.....	29
Figure 2-10. Temperature-dependent PL spectra of pristine MAPbBr ₃ and MAPbBr ₃ with ODT from 80 K (left) to 300 K (Right).....	29
Figure 2-11. Excitation-power-dependent PL spectra of pristine MAPbBr ₃ and MAPbBr ₃ with ODT at 80 K (upper) and 300 K (lower).....	30
Figure 2-12. (a) Device structure of PeLEDs. (b) Current density, (c) luminance, (d) current efficiency, and (e) EQE of PeLEDs as a function of applied voltage. (f) Relative luminance of the PeLEDs over time..	32
Figure 2-13. (a) Normalized EL spectrum of pristine and thiol-incorporated PeLEDs.....	33
Figure 2-14. (a) Current density, (b) current efficiency, (c) luminance of PeLEDs using pristine or thiol-incorporated MAPbBr ₃ based on FTO anode as a function of applied voltage. (d) Histogram of the current efficiency of the PeLEDs.....	33

Figure 3-1. . Illustration of candidate of cation for ideal mixed cation system...	46
Figure 3-2 Role of Cs : FA-Cs Mixed cation for PeLEDs.	47
Figure 3-3. Advantage of Guanidium cation for FA-based perovskite structure..	49
Figure 3-4. Structural analysis with changing GA cation ratio in FA-Cs system.	55
Figure 3-5 SEM analysis with different GA cation ratio (yellow mark are GA substitution ratio in FA-site).....	56
Figure 3-6 Uv-vis Absorption spectrum and structure model for FAPbBr ₃ and FA ₂ PbBr ₄ , absorption of stoichio control with FABr: PbBr ₂ ratio Copyright 2019, Royal Society of Chemistry. ²⁷	56
Figure 3-7 Optoelectronic properties with changing GA cation ratio in FA-Cs system.....	58
Figure 3-8. J-V-L Characteristics with changing GA cation in FA-CS system....	59
Figure 3-9. hole-only device results comparison between w/o GA and w/ GA. .	59
Figure 3-10. Tolerance factor and PL Intensity changes with MA & GA ratio. .	60
Figure 3-11. J-V-L Characteristics and lifetime analysis with different mixed cation system perovskite (e.g.; FA-Cs, FA-GA-Cs, FA-MA-GA-Cs).....	62
Figure 3-12. Histogram of EQE with quadruple cation PeLEDs..	62
Figure 4-1. Schematic overview of single-source 3D perovskite with BnABr co-deposition..	69
Figure 4-2. CsPbBr ₃ powder synthesis for the single-source perovskite films. .	75
Figure 4-3. TGA Analysis with CsPbBr ₃ powder and MAPbBr ₃ powder.....	75
Figure 4-4. TGA Analysis with CsPbBr ₃ powder with stoichiometric control.....	76
Figure 4-5. XPS Analysis with CsPbBr ₃ powder with stoichiometric control.	77

Figure 4-6. Photophysical properties of single-source vapor evaporation CsPbBr ₃ film.....	77
Figure 4-7. Photophysical properties of fine-stoichiometry control vapor evaporation CsPbBr ₃ film.....	78
Figure 4-8. Illustration of quasi-2D phase distribution, and steady-state PL and PL Lifetime analysis with Quasi-2D perovskite films, picture of different n value films under UV	80
Figure 4-9. 2D characteristics with XRD and UV-vis Absorption spectrum.....	81
Figure 4-10. SEM image of CsPbBr ₃ (3D) and CsPbBr ₃ with BnABr (Quasi-2D)	81
Figure 4-11. JVL-Characteristics with different n value of vapor-deposition Quasi-2D PeLEDs.	83
Figure 4-12. Histogram of CE with Quasi-2D PeLEDs.	84

Chapter 1. Introduction

1.1. Overview of Perovskites

Metal halide perovskites (MHP) are a rising field of semiconducting materials that show outstanding properties. Usually, perovskite structure is ABX_3 , which A and B are cations and X are anions. The $[BX_6]^{4-}$ octahedral 3D framework are formed, and small A-site cations are in the cavities. Especially, MHP have several characteristics for application in solar cells such as high absorption coefficients, long minority carrier diffusion lengths, and high charge-carrier mobilities. Therefore, lots of researcher have focused on these materials for perovskite solar cells (SCs).¹⁻³ For the ionic structure stability, the tolerance factor t is introduced. The ionic radius of ABX_3 is follow $r_A + r_X = \sqrt{2}(r_B + r_X)$. The tolerance should be $0.81 < t < 1.11$ for formed the perovskite structure (**Figure 1-1a**). Difference of structure change the properties of the materials, so different ration of cation and anion substitution have been used for changing physical and chemical properties. Usually, A-site cation is a monovalent cation (e.g., $CH_3NH_3^+$ (MA), $HC(NH_2)_2^+$ (FA), Cs^+), B-site cation is metallic cation (e.g., Pb^{2+} , Sn^{2+} , Ge^{2+} , Ca^{2+} , Mn^{2+} , Zn^{2+} , Mn^{2+} , etc), and X-site anion is a halide anion (e.g., I^- , Br^- , Cl^-). MHP's bandgap is dependent on the chemical bonding between the metal cation (B-site) and the halogen anion (X-site) that comes from difference of electronegativity.

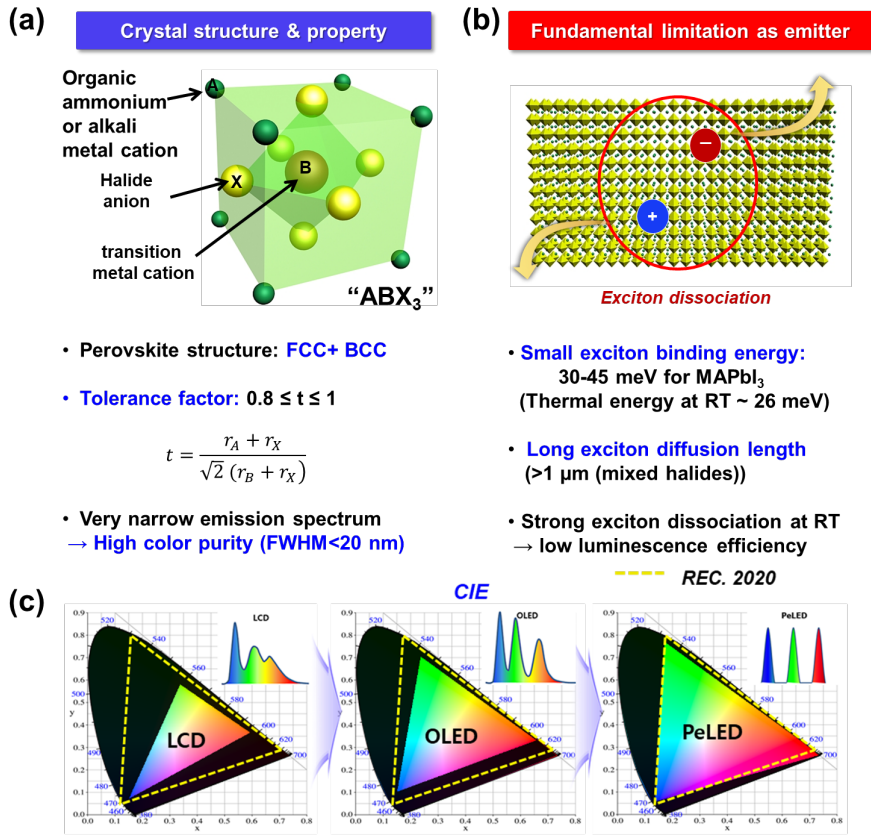


Figure 1-1 a) Structure properties b) Fundamental limitation as an emitter c) Emergence of future emitter with perovskite materials.

Most of the paper focused on the Pb-based perovskite for SCs and light-emitting diodes (LEDs) because of outstanding properties, but research on environmentally friendly B-site cation such as Sn²⁺, Ge²⁺ are insufficient until now. Several characteristics which was good for SCs such as small exciton binding energy, and long exciton diffusion length are bad for the LEDs because of strong exciton dissociation at room temperature (**Figure 1-1b**). Therefore, we should focus on the methods to overcome these properties without maintain advantages of perovskite materials. MHP have superior material properties for emitters: excellent photoluminescence (PL), narrow light emission (FWHM < 20nm), easy color tuning, and balanced charge carrier mobility (**Figure 1-1c**).^{4,5}

1.2. Dimensionality and Structure of Perovskites

One of the ways that change the optical properties of perovskites are modulation of dimensionality. This low-dimensional perovskite composition modification could change the opto-physical properties such as exciton binding energies and bandgap. The rigid ABX_3 structure are hardly modified due to BX_6 octahedral structure. However, low dimensional perovskites have structural flexibility influenced by the length of large organic cations.

Early perovskite research mainly deals with **Three-Dimensional Perovskites** (e.g., $MAPbI_3$).¹ This 3D perovskites show extremely low defect state compared to crystalline silicon, and long carrier diffusion lengths.⁶ However, the $MAPbI_3$ have severe instability problems against moisture and heat. Therefore, finding stable A-site cation are next step for the stability. Also, the modification of A-site cation controls the bandgap due to lattice constant change (FA is larger than MA, resulting in an increase of bandgap).⁷ FA cation have thermally stable properties than MA, but still have phase instability problems with $FAPbI_3$ perovskite. This has led to a introduction of mixed-cation system such as FA-Cs, FA-MA-Cs, and FA-MA-Rb not only for overcome phase instability, but also solve the instability against heat.⁸ The long excited state lifetimes and high PL characteristics are the reason of outstanding results of perovskite LEDs. Also, these characteristics are highly depending on the perovskite film quality. High-quality perovskite films, and grain boundaries are important parameter for opto-physical properties. Researchers have been studied the passivation of grain boundaries using various methods such as chemical treatment,^{9,10} additive engineering,^{11,12,13} and dimensionality control.^{14,15}

Longer-chain alkyl ammonium (A') than conventional 3D perovskite A-site cation

could make **Two-Dimensional (2D) Perovskites** which is expressed as an A'_2BX_4 . To control the low-dimensional perovskites, organic cation (A and A') and stoichiometric ratio are important factors. Especially, this change of dimensionality has impact on electronic properties of perovskites, especially the bandgap are increased with reducing dimensionality. Moreover, the low-dimensional perovskites are forming natural quantum-well structures, and they have large exciton binding energies (>100 meV).¹⁶ This quantum-well structure increase PL intensity and strong exciton confinement from diminished forbidden electronic transitions (**Figure 1-2**).

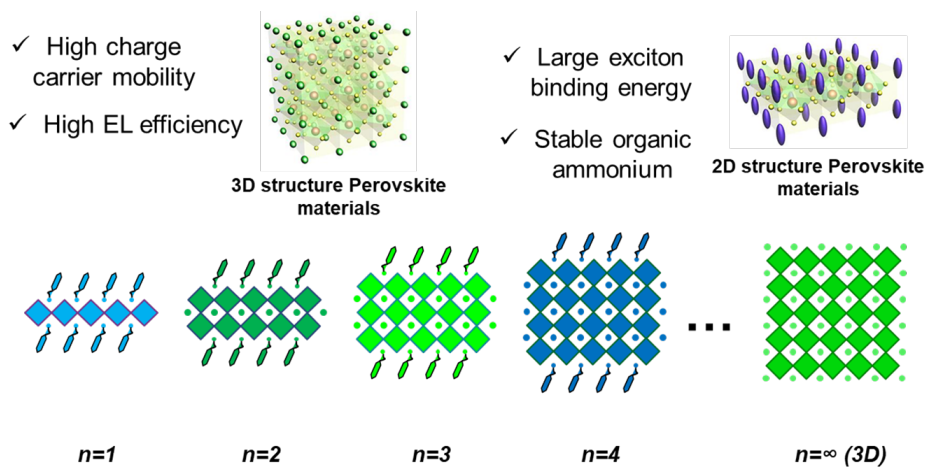


Figure 1-2 Illustration of benefit of low-dimensional Structure perovskite

More recently, Quasi-2D structure have been studied for LEDs application with these attractive characteristics.¹⁷ Higher number layered compounds ($A'_2A_{n-1}Pb_nX_{3n+1}$) with $n = 2, 3, 4$, etc. are formed through mixture of different cations, using mixed 3D and layered perovskite structures.^{14,18,19} By mixture of n value of perovskite structure, energy funneling effect are shown through a collection of grains having different bandgaps. Furthermore, this funneling effect and quantum-well structure make huge progress of luminescence properties in perovskite LEDs.^{15,17-19}

1.3. Vapor-deposition methods

MHP have great potential for the future display industry but commercializing of PeLEDs still have obstacle which are large-area technique and low-reproducibility. Thermal evaporation is most widely adopted technique in display industry. The principle of the technology is a chemical reaction with physical heating of the materials, and then the materials are vaporized under an ultra-high vacuum atmosphere. Especially, thermal deposition has several advantages compare with solution-processing (Figure 1-3).

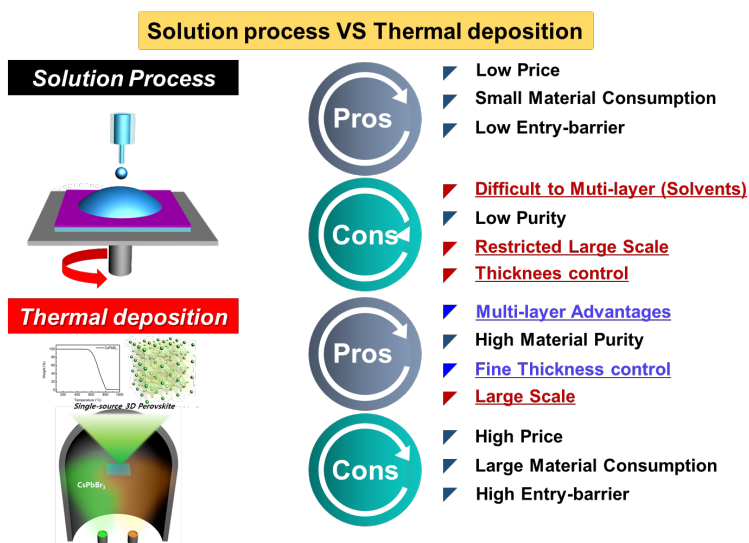


Figure 1-3 The difference between solution-processing and thermal deposition.

Thermal deposition is solvent-free process, so making multi-layer are much easier than solution-processing, also we could ignore solubility issue. For example, inorganic perovskite has difficult with high-coverage film formation.^{20,21} Easy and precise thickness,²² oxygen-sensitive or unstable perovskite are easily fabricated with high vacuum condition,²³ sublimation make the material purification, and result in low trap density,²⁴ high-reproducibility and easy-fabrication of large-area devices.

Two deposition techniques have been studied widely in perovskite fields such as

co-evaporation and sequential evaporation. Firstly, multisource co-evaporation is widely used for perovskite film because the different precursors are needed for formation of perovskite, and different crucible are needed for depositing perovskite film.²⁵ Two different precursors loaded in the separated crucible for depositing perovskite film.²⁶ The substrate shutter is controlled for optimized deposition rate, and then these two precursors are mixed on the substrate at the same time. Generally, rotation of substrate are introduced for the fully mixed composition perovskites though whole films.²⁷ Especially, we do not need the high temperature annealing for smooth and full coverage films, so we could choose the thermal unstable substrate which is used for flexible devices.²⁸ The different evaporation rate are key parameter for opto-physical properties of films.²⁴ Also, this precise reaction rate control are the advantage of the co-evaporation compared with another deposition methods.

In general, different precursors are evaporated layer by layer. We usually choose this evaporation technique when there are no multiple sources, or difficult to control the evaporation rate control because of too many precursors are needed (more than two). For example, double-halide perovskite ($\text{Cs}_2\text{AgBiBr}_6$) is needed three different sources for film formation, so we could simplify the evaporation by introducing sequential deposition.²⁹ However, film annealing or in-situ annealing of substrate are need for the formation of optimized perovskite films because, the reaction occurs after formation of one film. Repeating thin layer deposition methods are introduced for easy reaction into inter-diffusion of films.³⁰⁻³³

1.4. Research strategies

In this section, we briefly describe the research strategies of in this thesis (**Figure 1-4**). We divided the whole thesis into the different project, i) Ideal structure for efficient PeLEDs, and ii) Vapor deposited perovskite for efficient LEDs. Project one is focused on the solution-processing. We could control the crystal structure two main technique : additive(thiol derivative) engineering, and Ideal mixed-cation system that comes from introducing guanidium (GA) substitution. In first chapter, we could passivate exciton quenching of interface and inside crystal simultaneously. Second chapter, we introduce partial GA cation substitution as a new A-site cation for defect passivation, then ideal mixed-cation system (quadruple cation system) is used for defect passivation of 3D polycrystalline perovskites.

Project two is about Quasi-2D perovskite by thermal deposition methods. We introduce the thermal deposition methods for overcome the limitation of solution process engineering such as low-reproducibility and hardship to fabricating large-area devices. Moreover, we could make Quasi-2D perovskite using co-deposition of BnABr and CsPbBr₃ for efficient luminance characteristics.

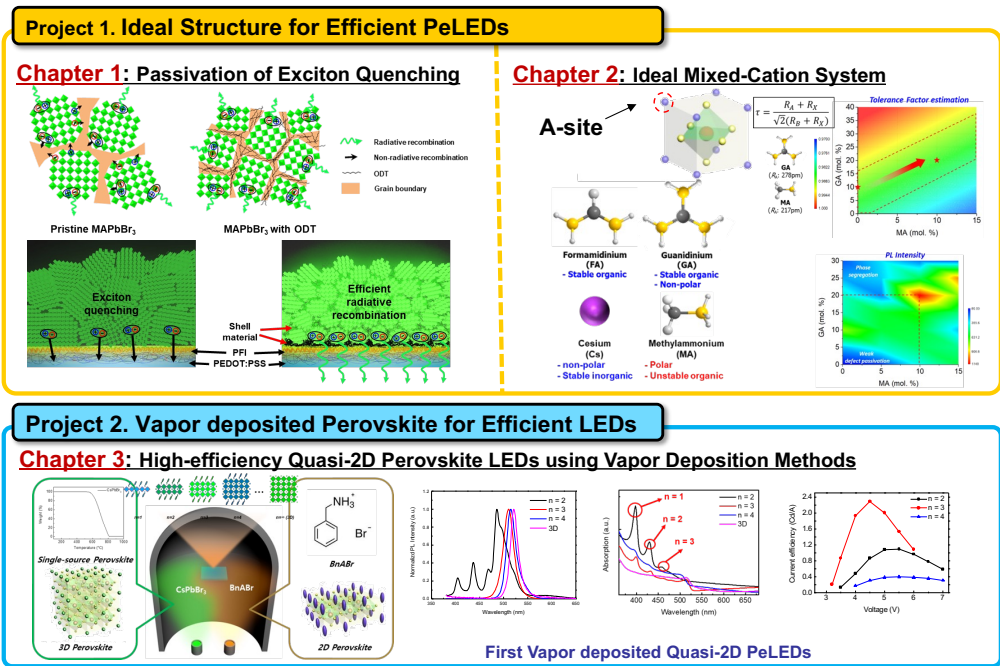


Figure 1-4 Illustration of research overview

1.5. Bibliography

1. Kojima, A., Teshima, K., Shirai, Y. & Miyasaka, T. Organometal Halide Perovskites as Visible-Light Sensitizers for Photovoltaic Cells. *J Am Chem Soc* **131**, 6050–6051 (2009).
2. Lee, M. M., Teuscher, J., Miyasaka, T., Murakami, T. N. & Snaith, H. J. Efficient hybrid solar cells based on meso-superstructured organometal halide perovskites. *Science (1979)* **338**, 643–647 (2012).
3. Liu, M., Johnston, M. B. & Snaith, H. J. Efficient planar heterojunction perovskite solar cells by vapour deposition. *Nature* **501**, 395–398 (2013).
4. Quan, L. N. *et al.* Perovskites for Next-Generation Optical Sources. *Chemical Reviews* **119**, 7444–7477 (2019).
5. Park, M.-H. *et al.* Boosting Efficiency in Polycrystalline Metal Halide Perovskite Light-Emitting Diodes. *ACS Energy Letters* **4**, 1134–1149 (2019).
6. Stranks, S. D. *et al.* Electron-hole diffusion lengths exceeding 1 micrometer in an organometal trihalide perovskite absorber. *Science (1979)* **342**, 341–344 (2013).
7. Byranvand, M. M. *et al.* Recent Progress in Mixed A-Site Cation Halide Perovskite Thin-Films and Nanocrystals for Solar Cells and Light-Emitting Diodes. *Advanced Optical Materials* **10**, 2200423 (2022).
8. Saliba, M. *et al.* Cesium-containing triple cation perovskite solar cells: improved stability, reproducibility and high efficiency. *Energy & Environmental Science* **9**, 1989–1997 (2016).
9. DeQuilettes, D. W. *et al.* Impact of microstructure on local carrier lifetime in perovskite solar cells. *Science (1979)* **348**, 683–686 (2015).

10. Hassan, Y. *et al.* Ligand-engineered bandgap stability in mixed-halide perovskite LEDs. *Nature* **591**, 72–77 (2021).
11. Zhao, B. *et al.* High-efficiency perovskite–polymer bulk heterostructure light-emitting diodes. *Nature Photonics* vol. 12 783–789 Preprint at <https://doi.org/10.1038/s41566-018-0283-4> (2018).
12. Cho, H. *et al.* Overcoming the electroluminescence efficiency limitations of perovskite light-emitting diodes. *Science (2015)* **350**, 1222–1225.
13. Park, M. *et al.* Efficient Perovskite Light-Emitting Diodes Using Polycrystalline Core–Shell-Mimicked Nanograins. *Advanced Functional Materials* **29**, 1902017 (2019).
14. Kim, H. *et al.* Proton-transfer-induced 3D/2D hybrid perovskites suppress ion migration and reduce luminance overshoot. *Nature Communications* **11**, 3378 (2020).
15. Yang, X. *et al.* Efficient green light-emitting diodes based on quasi-two-dimensional composition and phase engineered perovskite with surface passivation. *Nature Communications* **9**, 2–9 (2018).
16. Mitzi, D. B. Synthesis, Structure, and Properties of Organic–Inorganic Perovskites and Related Materials. *Progress in Inorganic Chemistry* **48**, 1–121 (2007).
17. Byun, J. *et al.* Efficient Visible Quasi-2D Perovskite Light-Emitting Diodes. *Advanced Materials* **28**, 7515–7520 (2016).
18. Xiao, Z. *et al.* Efficient perovskite light-emitting diodes featuring nanometre-sized crystallites. *nature.com*.
19. Yuan, M., Quan, L., Comin, R., ... G. W.-N. & 2016, undefined. Perovskite

- energy funnels for efficient light-emitting diodes. *nature.com*.
20. Cho, H. *et al.* High-Efficiency Solution-Processed Inorganic Metal Halide Perovskite Light-Emitting Diodes. *Advanced Materials* **29**, (2017).
 21. Heo, J.-M. *et al.* Bright Lead-Free Inorganic CsSnBr₃ Perovskite Light-Emitting Diodes. *ACS Energy Letters* 2807–2815 (2022) doi:10.1021/ACSENERGYLETT.2C01010.
 22. Hsiao, S.-Y. *et al.* Efficient all-vacuum deposited perovskite solar cells by controlling reagent partial pressure in high vacuum. *Wiley Online Library* **28**, 7013–7019 (2016).
 23. Zhang, J., Hodes, G., Jin, Z. & Liu, S. All-Inorganic CsPbX₃ Perovskite Solar Cells: Progress and Prospects. *Angewandte Chemie – International Edition* **58**, 15596–15618 (2019).
 24. Ávila, J., Momblona, C., Boix, P. P., Sessolo, M. & Bolink, H. J. Vapor-Deposited Perovskites: The Route to High-Performance Solar Cell Production? *Joule* **1**, 431–442 (2017).
 25. Chiang, Y. H., Anaya, M. & Stranks, S. D. Multisource Vacuum Deposition of Methylammonium-Free Perovskite Solar Cells. *ACS Energy Letters* **5**, 2498–2504 (2020).
 26. Hu, Y. *et al.* Vacuum-evaporated all-inorganic cesium lead bromine perovskites for high-performance light-emitting diodes. *pubs.rsc.org*.
 27. Du, P. *et al.* Vacuum-Deposited Blue Inorganic Perovskite Light-Emitting Diodes. *ACS Applied Materials and Interfaces* **11**, 47083–47090 (2019).
 28. Zhao, D. *et al.* Annealing-free efficient vacuum-deposited planar perovskite solar cells with evaporated fullerenes as electron-selective layers. *Elsevier*.

29. Wang, M. *et al.* High-Quality Sequential-Vapor-Deposited Cs₂AgBiBr₆ Thin Films for Lead-Free Perovskite Solar Cells. *Wiley Online Library* **2**, (2018).
30. Ling, Y. *et al.* Composite Perovskites of Cesium Lead Bromide for Optimized Photoluminescence. *Journal of Physical Chemistry Letters* **8**, 3266–3271 (2017).
31. Akman, E., Shalan, A. E., Sadegh, F. & Akin, S. Moisture-Resistant FAPbI₃ Perovskite Solar Cell with 22.25 % Power Conversion Efficiency through Pentafluorobenzyl Phosphonic Acid Passivation. *ChemSusChem* **14**, 1176–1183 (2021).
32. Jia, K. *et al.* Improved Performance for Thermally Evaporated Perovskite Light-Emitting Devices via Defect Passivation and Carrier Regulation. *ACS Applied Materials and Interfaces* **12**, 15928–15933 (2020).
33. Lin, H. Y. *et al.* Efficient Cesium Lead Halide Perovskite Solar Cells through Alternative Thousand-Layer Rapid Deposition. *Advanced Functional Materials* **29**, (2019).

Chapter 2. Multifunctional Dithiol Additive in Polycrystalline Perovskite Emitters for Suppression of Non-Radiative Recombination

2.1. Introduction

Perovskite light-emitting diodes (PeLEDs) have become the focus of interest based on promising properties of the perovskites as a light emitter such as high brightness, high color purity, and easy color tunability.¹⁻⁶ Also, outstanding optoelectronic properties of perovskites based on high defect tolerance enabled their efficient radiative recombination and high luminous efficiency.^{1,7} Thus, PeLEDs have achieved external quantum efficiency (EQE) over 20% in green,⁸⁻¹⁰ red,¹¹⁻¹³ and infra-red.¹⁴⁻¹⁷ Nevertheless, defect-induced traps in perovskites can still prevent efficient radiative recombination and limit device characteristics of PeLEDs in terms of efficiency and stability.¹⁸⁻²² Due to the ionic nature of the defects, their influence on recombination dynamics and structural stability of perovskites becomes more significant under an electric field.^{23,24} To be specific, the ions can accumulate at the interface of perovskites with an adjacent layer, in particular, a hole-injection layer (HIL) during the operation of PeLEDs as the negatively charged halide ion is the dominant defect within perovskites.^{25,26} Therefore, charge trapping and quenching via non-radiative recombination can occur more easily at the interface.^{23,27} Also, the accumulated ions can aggravate operational stability of PeLEDs by increasing a local electric field at the interface.²⁸ Therefore, defect passivation of perovskites and suppression of non-radiative recombination dynamics are essential to the demonstration of efficient and stable PeLEDs.

Various strategies of defect passivation have been reported to mitigate the negative impact of defects on charge carrier dynamics and stability of perovskites.^{29,30} The majority of them are based on Lewis-base passivation of under-coordinated Pb^{2+} that is correlated with the halide vacancy.³¹ The molecules including nitrogen, sulfur, oxygen or phosphorus which can donate lone pair electrons have exhibited effective passivation of the under-coordinated Pb^{2+} by neutralizing the perovskite lattice.^{23,32–34} Thus, it can prevent undesirable non-radiative recombination at the corresponding trap sites, and also help maintain the structural integrity of perovskites.

In addition to the defect passivation, spatial confinement of excitons is one of the keys to efficient radiative recombination. For example, a breakthrough in PeLED characteristics was achieved by the introduction of the nanocrystal pinning (NCP) method that led to a reduction of grain size and well-confined excitons in the grains.^{18,35} On the other hand, a self-organized exciton buffer layer composed of a hole-injection material poly(3,4-ethylenedioxythiophene) polystyrene sulfonate (PEDOT:PSS) and a perfluorinated ionomer (PFI) was proven to be useful for blocking exciton quenching at the interface.³⁶

In this study, we introduce a dithiol reagent, 1,8-octanedithiol (ODT), in methylammonium lead bromide (MAPbBr_3) for a multifunctional role in defect passivation of the perovskite, spatial confinement of excitons, and reduction of exciton quenching at the interface. The nucleophilic thiol can be particularly useful for Lewis-base passivation of under-coordinated Pb^{2+} in MAPbBr_3 (**Figure 2-1a**). Also, the additive can surround perovskite grains where excitons can be spatially confined inside the grains (**Figure 2-1b**). Furthermore, due to the distribution of the

additive dominantly at the lower part of the perovskite layer, exciton quenching at the interface between the perovskite and the underlying HIL can be reduced (**Figure 2-1c**). Enhanced carrier dynamics of the perovskites with the additive are revealed by photoluminescence (PL) studies. PeLEDs using the thiol-incorporated polycrystalline emitter based on a conducting polymer anode (CPA) containing the self-organized exciton buffer layer exhibited a highly improved external quantum efficiency (EQE) and an extended operational lifetime (EQE: 14.2% and T_{50} : 139 min) compared to the otherwise-identical device using pristine polycrystalline emitter (EQE: 8.7% and T_{50} : 59 min). To the best of our knowledge, this is the highest EQE of PeLEDs among polycrystalline MAPbBr₃ emitters (**Table 1-1 and Figure 2-2**).

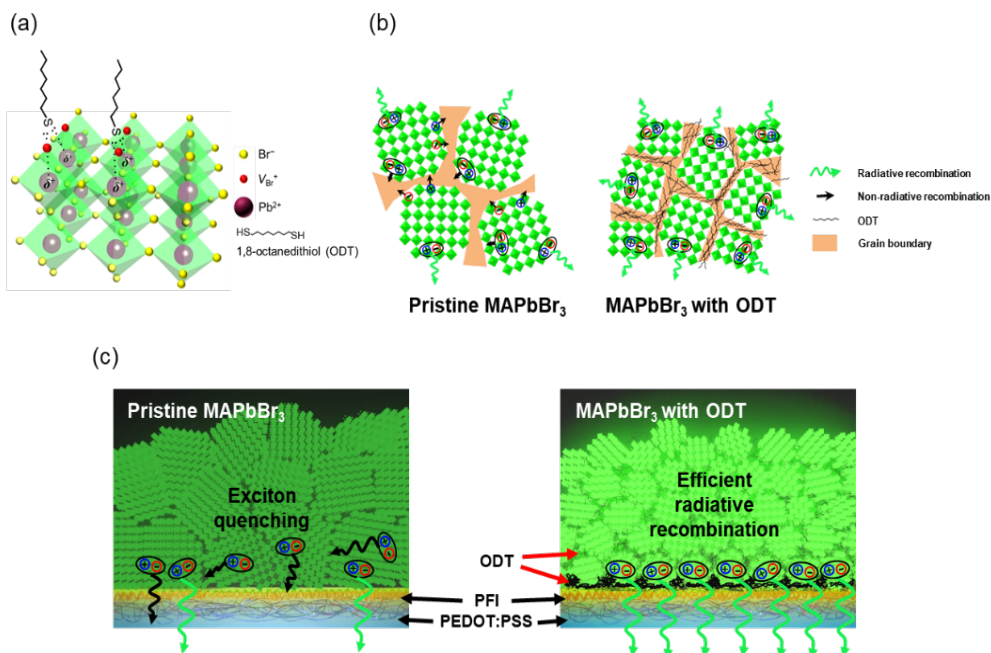


Figure 2-1. Schematic illustrations of (a) Lewis-base passivation of undercoordinated Pb²⁺ by ODT, (b) spatial confinement of exciton inside grains

by ODT, and (c) efficient radiative recombination with the use of ODT that prevents exciton quenching at the interface of perovskite/HIL.

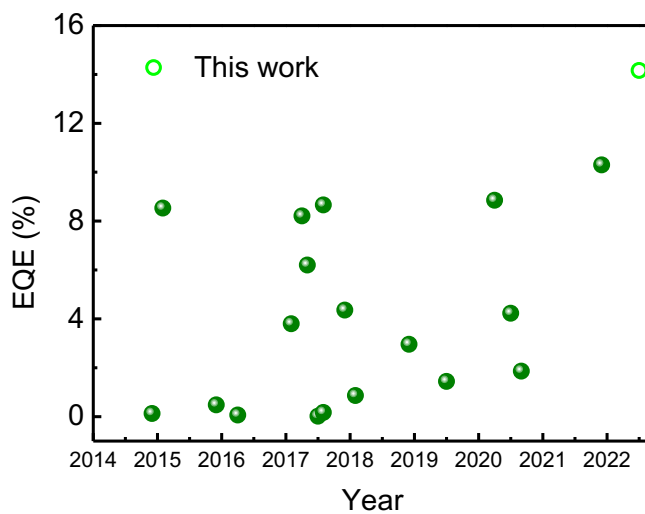


Figure 2-2. EQE developments of the reported PeLEDs that are used MAPbBr₃ as an emitter.

2.2. Materials and Experiments

Preparation of perovskite solutions

CH₃NH₃Br (MABr) (Dyesol) and PbBr₂ (Aldrich) (1.08:1 molar ratio) were dissolved (1.2M) in dimethyl sulfoxide (DMSO) (Aldrich). For the incorporation of thiol, 10 vol % of 1,8-octanedithiol (ODT) (Aldrich) was added to the MAPbBr₃ precursor solution, and the solution was vigorously stirred.

PeLEDs fabrication

Glass substrates were used after cleaning by sonication with acetone and isopropanol. As an anode, 100-nm-thick self-organized conducting polymer (CPA) was spin-coated as previous papers.³⁷ The spin-coated CPA films were annealed at 200 °C for 10 min in ambient. On top of the CPA layer, the perovskite films were deposited by spin-coating the precursor solutions in a nitrogen-filled glove box. During the spin-coating, NCP process was applied using TPBi solution in chloroform (0.1 wt. %). The perovskite films were annealed at 70 °C for 10 min, then the samples were loaded into a high-vacuum chamber ($< 10^{-7}$ Torr) and then TPBi (45 nm), LiF (1 nm), and Al (100 nm) were thermally evaporated as an electron transport layer, injection layer, and cathode layer, respectively. The devices were encapsulated by a glass lid using UV-curable resin.

Device characterization

All the devices were measured after encapsulation in N₂ atmosphere. The current-voltage-luminance characteristics of PeLEDs were measured as described in our

previous work using a computer-controlled source-measurement unit (Keithley 236) and a spectroradiometer (Minolta CS2000).³⁸

¹H NMR measurement

We used a high-resolution NMR spectrometer (Bruker Advance 600 MHz) to obtain the ¹H NMR spectra. For the pristine perovskite precursor, MABr and PbBr₂ were dissolved in DMSO-*d*₆ (0.02 M) and the CSMP solution was prepared by adding 10 vol% of ODT in the pristine solution. Pristine ODT was also prepared at the same concentration as the perovskite solution in DMSO-*d*₆ for comparison. All the samples were prepared at room temperature in N₂ atmosphere and measured at room temperature.

Steady-state PL measurement

The steady-state PL of MAPbBr₃ layers on Glass/CPA was measured using a spectrofluorometer (JASCO FP8500).

Time-correlated single-photon counting measurement

The PL decay of MAPbBr₃ films on glass/CPA was investigated using a TCSPC system. A pulsed diode-laser head (PicoQuant, LDH-D-C-405) coupled with a laser-diode driver (PicoQuant, PDL 800-D) was used as an excitation source. The excitation wavelength was 405 nm. The fluorescence was spectrally resolved using a monochromator (Acton, SP-2155) and its time-resolved signal was measured by a TCSPC module (PicoQuant, PicoHarp) equipped with a microchannel plate photomultiplier tube (Hamamatsu, MCP-PMT, R3809U-50,). The PL decay was

measured at 545 nm. To calculate the fluorescence lifetime from actual decay signal, the output curve was deconvoluted using FluoFit (PicoQuant).

Temperature- and Excitation power-dependent PL measurement

The temperature of the samples was controlled by a liquid-nitrogen cryostat (Oxford instruments DN2, sample in exchange gas) using an Oxford instruments Mercury iTC. The sample temperature is read from a single sensor and is believed to be accurate within 1K according to manufacturer specifications. As an excitation light source, a 405 nm continuous-wave laser diode (PicoQuant, LDH-D-C-405) was used and the emitted light was collected using a fiber-coupled stellar Net blue-wave spectrometer. The laser power was varied using a laser-driver (PicoQuant, PDL 800-D) from 3 to 58 mW which was confirmed by a laser power meter (Thorlabs, PM100D).

Transmission electron microscopy (STEM)

Lamella for STEM-EDX analysis were prepared by conventional focused ion beam lift-out using a Zeiss NVision40. High-angle annular dark-field (HAADF) STEM imaging and energy dispersive X-ray spectroscopy (EDXS) were performed on a Thermo Fisher Titan-Themis 60-300, equipped with a high brightness Schottky X-FEG gun, four silicon drift Super-X EDX detectors, and Velox acquisition software. EDX data were collected in the form of spectrum images, in which a focused electron probe was scanned in raster (1024×1024 pixels) across a region of interest in the scanning TEM (STEM) mode. For each scan point, structural information was obtained from the electron scattering incident on a high-angle annular dark-field detector, and simultaneously, an EDX spectrum was obtained by

collecting X-rays emitted from the local volume probed by the electron beam. Spectrum images were acquired with a probe current of approximately 250 pA at an acceleration voltage of 200 kV.

2.3. Results and Discussion

We used 10 vol % of ODT in the MAPbBr₃ precursor solution, and we performed liquid-state ¹H nuclear magnetic resonance (NMR) spectroscopy of the solution in comparison to the pristine MAPbBr₃ and ODT per se to investigate the underlying chemistry in the precursor state (**Figure 2-3a**). The solutions for the NMR spectroscopy were prepared in dimethyl sulfoxide-d₆ (DMSO-d₆) to keep the chemical environment and concentration the same as for the actual film fabrication. The spectrum of pristine MAPbBr₃ exhibited two dominant proton signals at $\delta = 7.53$ and 2.37 ppm that represent the ammonium ($-\text{NH}_3^+$) and the methyl ($-\text{CH}_3$) group of methylammonium (MA), respectively. On the other hand, the spectrum of ODT showed discrete peaks as denoted from (a) to (e) according to the position of the protons within the molecule. The addition of ODT to the pristine MAPbBr₃ solution caused a broadening of the proton signal of the ammonium group (denoted as g) due to the increasing acidity of the solution (**Figure 2-4**).³⁹ Also, the proton signals by ODT itself arose. However, the proton signal of the thiol group (indicated as a) notably exhibited a downfield shift from 2.154 to 2.158 ppm indicating deshielding of the thiol moiety while the rest of the proton signals of CH₂ within ODT resulted in an upfield shift (**Figure 2-5**). We may attribute the deshielding to Lewis-base-acid interaction between the thiol and Pb²⁺ based on a strong nucleophilicity of the thiol group.

The MAPbBr₃ films were prepared by spin-coating with the NCP process using 2,2',2''-(1,3,5-benzinetriyl)-tris(1-phenyl-1-H-imidazole) (TPBi) in chloroform.^{18,40} The presence of ODT in the precursor led to the formation of smaller grains of MAPbBr₃ that can be more favorable to spatial confinement of excitons

than the pristine MAPbBr₃ (**Figure 2-6**).^{8,41} Dynamic secondary ion mass spectrometry (DSIMS) depth profile of the thiol-incorporated MAPbBr₃ film revealed a gradual increase in the sulfur intensity toward the substrate side, which indicates that the thiol compound is dominantly distributed at the bottom region of the film (**Figure 2-3b**). In contrast, a negligible sulfur signal was observed in the pristine perovskite film. High-angle annular dark-field scanning transmission electron microscopy (HAADF-STEM) corroborated the distribution of ODT within the film. **Figure 2-3c** shows a cross-sectional view of the interface region from the HIL to the perovskite layer and we observed a discernible contrast among the areas as indicated in the red boxes; area #1, #2, and #3 illustrate a region of MAPbBr₃, the ODT compound, and the HIL, respectively. The integrated energy-dispersive X-ray spectroscopy (EDX) spectrum of each area represents the presence of peaks for Pb and S in the three areas. Given the similar intensity of Pb-M β between areas #1 and #2, we can assign those areas to the perovskite layer. Notably, the dominant peak of the area #2 spectrum exhibited a shift to lower energy, which can be attributed to the inclusion of the sulfur containing ODT in the area. In contrast, the spectrum of area #3 showed a reduction of Pb-M β intensity while its major peak chiefly arose from an increasing intensity of S-K due to PEDOT:PSS. Thus, based on the results of DSIMS and STEM-EDXS analyses, we can conclude the ODT compound is gradually distributed along the perovskite layer from its interface with the HIL. Despite the incorporation of ODT in the perovskite layer, X-ray diffraction (XRD) of the film did not show a significant change in its pattern from that of pristine perovskite film (**Figure 2-7**). This indicates that the addition of ODT did not deform the crystalline structure of MAPbBr₃. Instead, it is more likely that the ODT

compound surrounds the grains and occupies grain boundary, which may enable excitons to be well confined inside the grains.

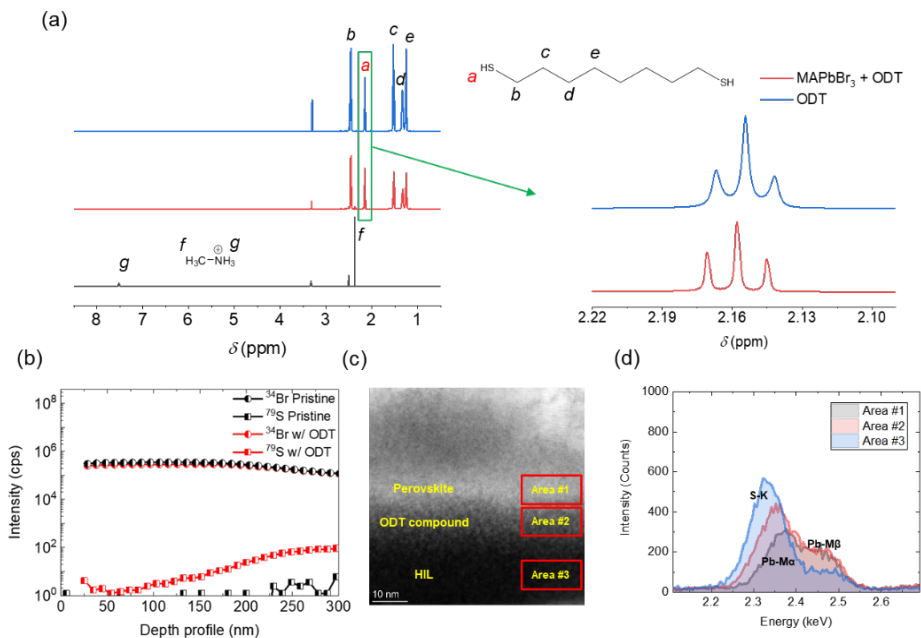


Figure 2-3. (a) ^1H NMR spectra of MAPbBr_3 (black), MAPbBr_3 with ODT (10 vol%) (red) in DMSO-d_6 , and pure ODT (blue). (b) DSIMS depth profile of perovskite films. Distributions of S and Br in PP MAPbBr_3 (black) and CSMP MAPbBr_3 (red). (c) HAADF scanning STEM cross-section image of thiol-incorporated perovskite film. (d) Integrated EDX spectra of the acquired data from the red boxed areas in (c).

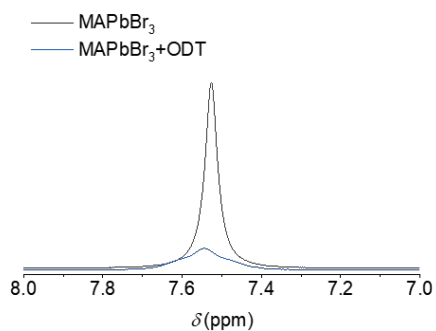


Figure 2-4. ^1H NMR spectra of pristine MAPbBr_3 (black) and MAPbBr_3 with ODT (10 vol%) (blue) in DMSO-d_6 .

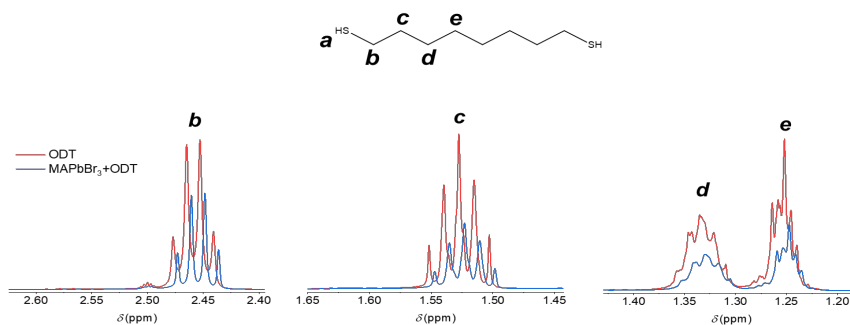


Figure 2-5. ^1H NMR spectra of MAPbBr_3 with ODT (10 vol%) (blue) and pristine ODT (red) in DMSO-d_6 showing signals of proton bonded to carbon within ODT as correspondingly denoted.

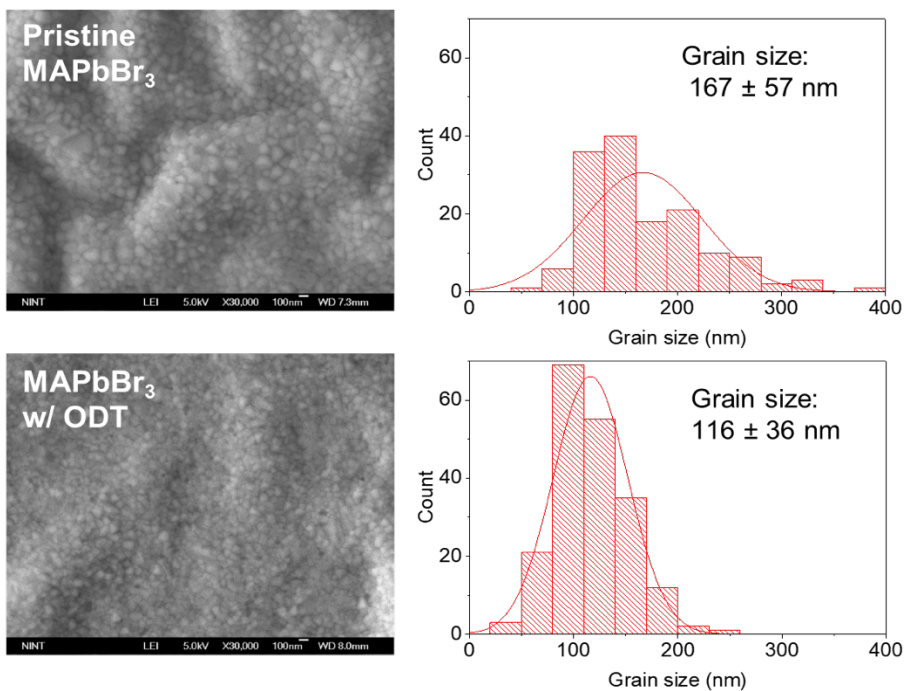


Figure 2-6. SEM images of pristine MAPbBr₃ and thiol-incorporated MAPbBr₃ films and corresponding grain size distribution.

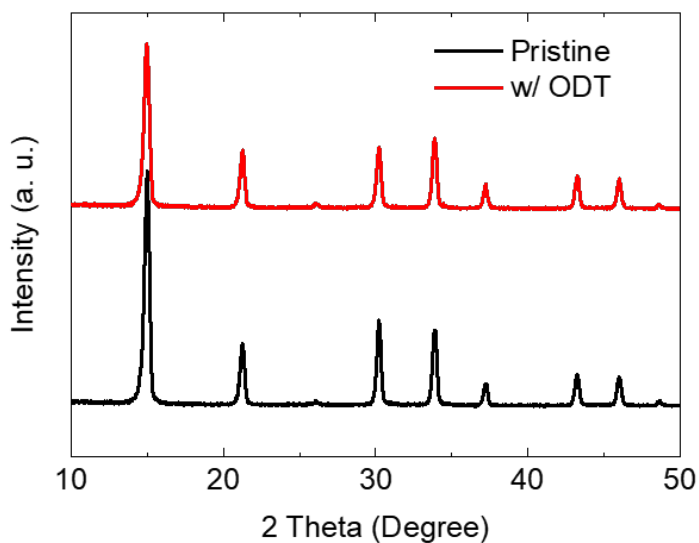


Figure 2-7. XRD pattern of pristine MAPbBr₃ (black) and MAPbBr₃ with the incorporation of ODT (red).

We performed various photoluminescence (PL) characterizations of the developed films to investigate the effects of the ODT compound. The thiol-incorporated MAPbBr₃ film exhibited a higher intensity of steady-state PL than the control film (**Figure 2-8a and b**). Nevertheless, the intensity difference was more noticeable when the films were excited from the bottom side of the substrate. This behavior can be explained by the gradual distribution profile of the ODT compound within the film as characterized by the DSIMS and HAADF-STEM above. We also performed transient PL measurement using time-correlated single-photon counting (TCSPC) (**Figure 2-8c**). The PL decay curves were fitted to bi-exponential decay function, $y = A_1e^{-t/\tau_1} + A_2e^{-t/\tau_2}$ where τ_1 and τ_2 are the lifetimes for the fast and slow decays, respectively. The thiol-incorporated perovskite exhibited a significant increase in PL average lifetime ($\tau_{\text{Ave}} = 185.82$ ns) compared to that of the pristine film ($\tau_{\text{Ave}} = 105.98$ ns). The detailed decay parameters are summarized in **Table 2-2**. The enhanced PL characteristics of the thiol-incorporated perovskite can be attributed to the effectively suppressed non-radiative recombination based on the multi-contribution of the ODT compound. 1) Under-coordinated Pb²⁺ formed by bromide vacancy (VBr⁺) on the grain boundary of MAPbBr₃ can be passivated by Lewis-base ODT to neutralize the lattice and subsequently annihilate corresponding defect states.⁴² 2) The insulating ODT compound that surrounds the grains can spatially confine excitons inside the grains suppressing their quenching at the grain boundary.⁴³ Given the distribution profile of ODT and the difference in the steady-state PL intensity according to the direction of light illumination, the defect passivation, and the spatial confinement can be dominantly effective at the lower part of the perovskite layer. 3) Furthermore, the ODT compound distributed at the bottom region of the perovskite layer can act as an additional buffer layer on the self-

organized conducting polymer (PEDOT:PSS:PFI) to block exciton quenching at their interface.

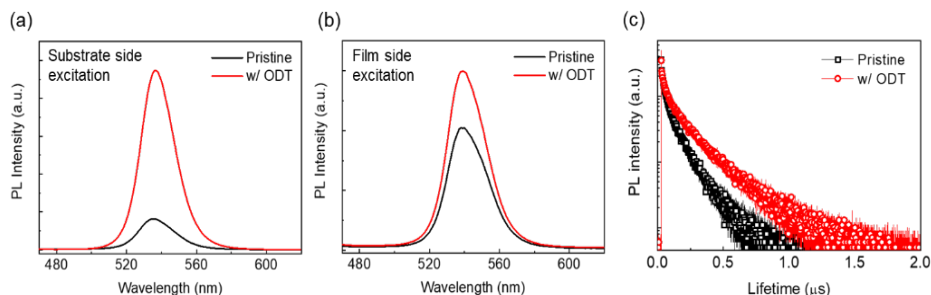


Figure 2-8. Steady-state PL spectrum of thiol-incorporated MAPbBr₃ (red) and pristine MAPbBr₃ (black) excited (a) from the substrate side and (b) from the film side. (c) Transient PL decay curves of the films.

Analysis of temperature-dependent integrated PL intensity of the films gives more specific information about recombination dynamics (**Figure 2-9a and 2-10**).⁴⁴

The intensity curves were fitted to an Arrhenius formula

$$I(T) = \frac{I_0}{1 + Ae^{-E_a/(k_B T)}}$$

where $I(T)$ is the integrated PL intensity as a function of temperature T , I_0 is $I(T)$ at $T = 0$, and k_B is the Boltzmann constant. E_a is the activation energy for the effective thermal activation process that leads to non-radiative recombination. By fitting the curves, we obtained $E_a = 236.2 \pm 7.0$ meV for the thiol-incorporated MAPbBr₃, and $E_a = 128.0 \pm 3.6$ meV for the pristine MAPbBr₃; the difference indicates that the occurrence of non-radiative recombination demands much higher energy in the thiol-incorporated MAPbBr₃ because the thiol compound globally contributed to the defect passivation, spatial confinement of exciton, and prevention of exciton-quenching at the interface, which facilitated radiative recombination.

The effect of ODT was also investigated by analysis of excitation-power-dependent PL intensity (I) of the perovskite films at 80 K and 300 K (**Figure 2-9b, c, and 2-11**). As PL of perovskite is dominated by near-band-edge emission, its intensity (I) follows a power-law dependence on excitation power (P) as $I = P^k$ and recombination processes can be assorted according to the k values;⁴⁵ Free- and bound-exciton radiative recombination has $1 < k < 2$, and a donor or an acceptor level-mediated recombination has $k < 1$. In other words, a lower k accounts for a higher density of trap states. At 80 K, the thiol-incorporated MAPbBr₃ had $k = 1.77 \pm 0.05$, and pristine MAPbBr₃ had $k = 1.65 \pm 0.02$. For both perovskites, thus, free- and bound-exciton radiative recombination were dominant for emission, but the slightly higher k of the thiol-incorporated MAPbBr₃ accounts for a lower density of trap states due to the defect passivation. Although both curves showed a change in the power-law at 300 K as increasing the excitation power, the thiol-incorporated MAPbBr₃ had $k = 1.62 \pm 0.10$ and the pristine MAPbBr₃ had 1.33 ± 0.08 where the power-law was maintained constant ($P < \sim 15$ mW). The power law in both films was lower than that at 80 K as more trap states can be thermally activated at 300 K. Nevertheless, the smaller reduction of k with the employment of the thiol compound can be indicative of a lower trap density by defect passivation than the pristine film. The saturation of both curves with the increase in P can be attributed to the trap filling.⁴⁶

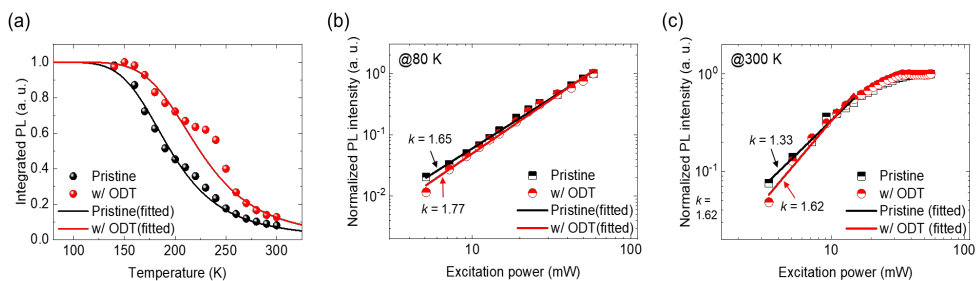


Figure 2-9. (a) Temperature-dependent integrated PL intensity of pristine and thiol-incorporated MAPbBr₃ films. Solid lines are fits to the data using the Arrhenius equation. Excitation-power dependent normalized PL intensity at (b) 80 K and (c) 300 K. Solid lines are linear fits to the data with a power-law k .

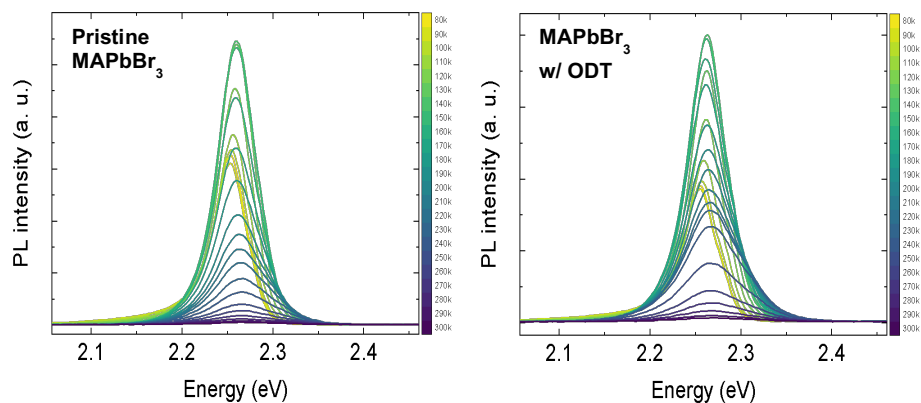


Figure 2-10. Temperature-dependent PL spectra of pristine MAPbBr₃ and MAPbBr₃ with ODT from 80 K (left) to 300 K (Right).

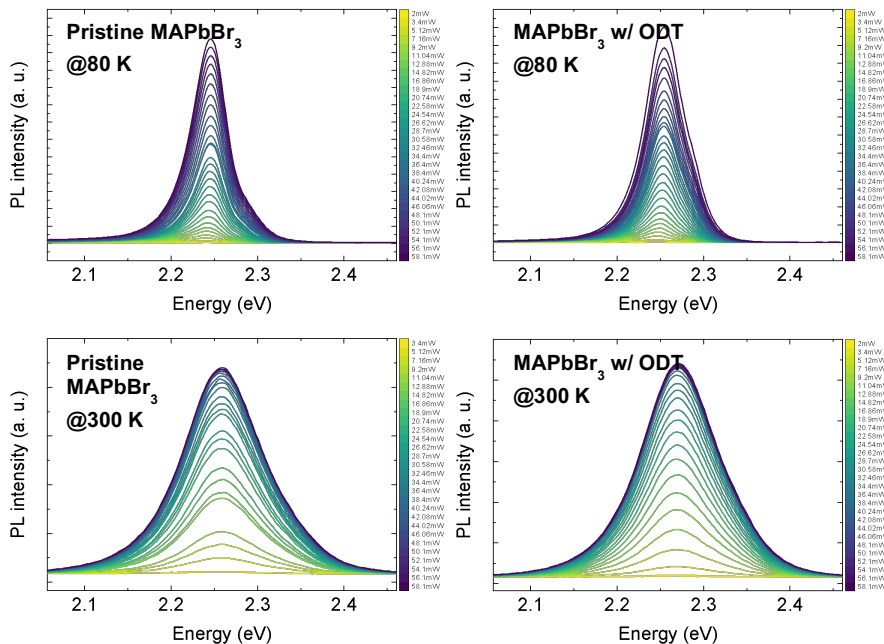


Figure 2-11. Excitation-power-dependent PL spectra of pristine MAPbBr₃ and MAPbBr₃ with ODT at 80 K (upper) and 300 K (lower).

We used the pristine and the thiol-incorporated MAPbBr₃ films as an emitter of PeLEDs. The device structure was CPA (100 nm)/perovskite (400 nm)/TPBi (50 nm)/LiF (1 nm)/Al (100 nm) as shown in **Figure 2-12a**. Current density-voltage (J-V) characteristics of the devices showed a similar behavior but the device using the thiol-incorporated MAPbBr₃ exhibited improved luminous characteristics (maximum luminance $L_{\max} = 15381 \text{ cd m}^{-2}$ and maximum current efficiency $CE_{\max} = 67.32 \text{ cd A}^{-1}$) compared to the device using the pristine MAPbBr₃ ($L_{\max} = 10130 \text{ cd m}^{-2}$ and $CE_{\max} = 40.67 \text{ cd A}^{-1}$) (**Figure 2-12b-d**). Both devices exhibited peak electroluminescence (EL) emission at 541 nm (**Figure 2-13**). The device with the thiol-incorporated MAPbBr₃ achieved maximum external quantum efficiency $EQE_{\max} = 14.16 \%$ which was significantly higher than the device with the pristine MAPbBr₃ (8.69 %) (**Figure 2-12e**). The improvement in the EL characteristics can be attributed to the passivation of the under-coordinated Pb²⁺, spatial confinement of

exciton, and exciton quenching blocking at the interface by the ODT compound. Also, we demonstrated the PeLEDs using FTO anode and presented statistics of CE_{\max} in which the thiol-incorporated perovskite exhibited its superiority to the pristine perovskite (**Figure 2-14 and Table 2-3**). Furthermore, the PeLEDs using the thiol-incorporated $MAPbBr_3$ emitter resulted in better operational stability than the control device under constant current to elicit initial luminance of 100 cd m^2 (**Figure 2-12f**). The thiol-incorporated PeLED exhibited a highly extended operational lifetime ($T_{50} = 139 \text{ min}$) compared to the pristine PeLED ($T_{50} = 59 \text{ min}$). We also attribute the improvement in the device stability to the ODT compound that may enhance the structural integrity of perovskites by defect passivation. Furthermore, the ODT compound distributed at the interface may act as a buffer layer to alleviate possible degradation at the interface by the ionic defect accumulation.

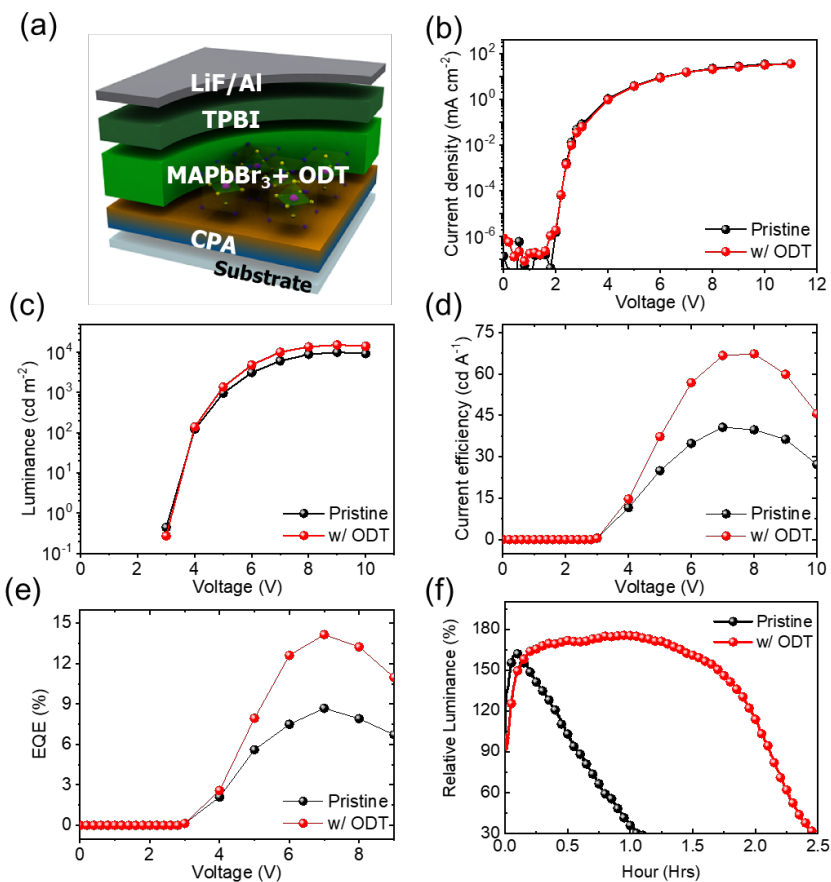


Figure 2-12. (a) Device structure of PeLEDs. (b) Current density, (c) luminance, (d) current efficiency, and (e) EQE of PeLEDs as a function of applied voltage. (f) Relative luminance of the PeLEDs over time.

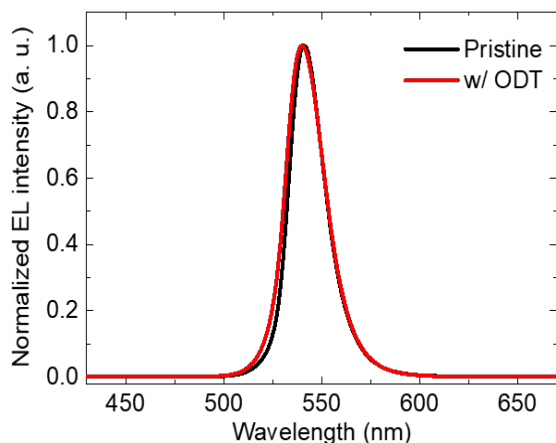


Figure 2-13. Normalized EL spectrum of pristine and thiol-incorporated PeLEDs.

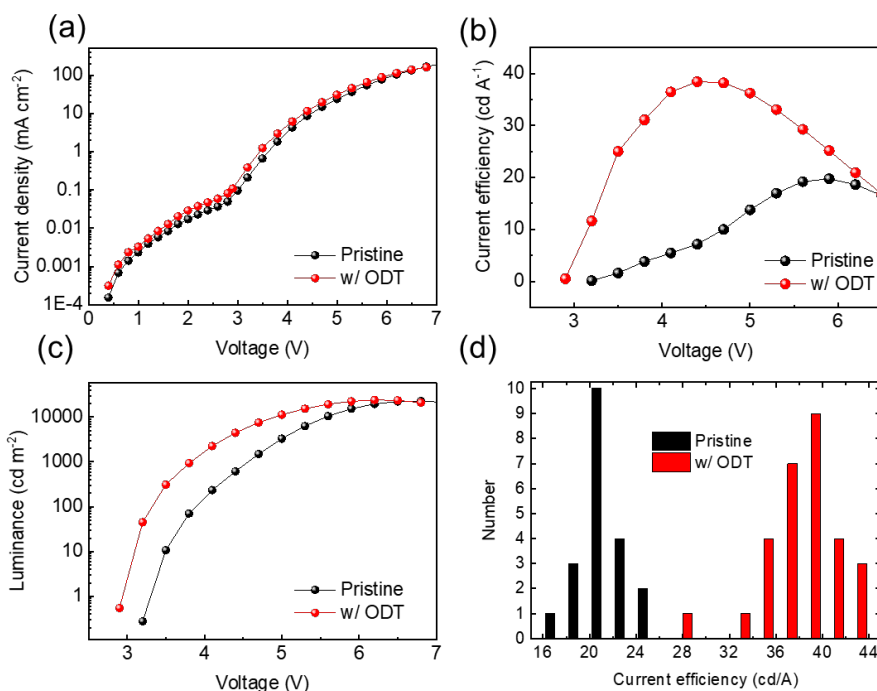


Figure 2-14. (a) Current density, (b) current efficiency, (c) luminance of PeLEDs using pristine or thiol-incorporated MAPbBr₃ based on FTO anode as a function of applied voltage. (d) Histogram of the current efficiency of the PeLEDs.

2.4. Conclusion

In conclusion, we used a multifunctional dithiol-based additive, ODT for defect passivation of MAPbBr₃, spatial confinement of excitons inside MAPbBr₃ grains, and reduction of interfacial exciton quenching between MAPbBr₃ layer and the underlying HIL. Under-coordinated Pb²⁺ in MAPbBr₃ was passivated by the Lewis-base ODT that can neutralize the defect and annihilate the corresponding defect states. Also, excitons can be spatially confined inside the grains by the ODT compound that surrounded the grains. Moreover, exciton quenching at the interface between the perovskite layer and the underlying HIL was inhibited due to the presence of the abundant ODT compound that might act as an additional buffer layer suppressing non-radiative recombination. Thus, the enhanced recombination dynamics by using the ODT compound in MAPbBr₃ were revealed by various PL studies. Finally, we demonstrated that the use of the thiol compound improved the luminous characteristics and operational stability of PeLEDs. We highlight that the use of nucleophilic thiol compound opens an intriguing prospect for the global impact on the effective suppression of non-radiative recombination for further research in the field of PeLEDs.

Table 2-1. Summary of the reported PeLEDs using MAPbBr₃ emitter.

Year	Device structure	EQE (%)	Current efficiency (cd A ⁻¹)	L_{max} (cd m ⁻²)	Ref.
2014.11	ITO/Buf-HIL/Perovskite/TPBI/LiF/Al	0.125	-	417	36
2015.10	SOCP/Perovskite/TPBI/LiF/Al	8.53	-	~10,000	18
2015.11	ITO/PEDOT/Perovskite/PBD/BCP/LiF/Al	0.48	-	10,590	47
2016.03	ITO/ZnO/Perovskite/PEDOT/Au	0.0645	-	196	48
2016.07	ITO/PEDOT/Perovskite/TPBI/LiF/Al	-	5.1	8,794	49
2017.01	Graphene/Buf-HIL/Perovskite/TPBI/LiF/Al	3.8	-	13,000	50
2017.03	ITO/PEDOT/Perovskite/BCP/LiF/Al	8.21	-	6,950	51
2017.04	ITO/PEDOT/Perovskite/SPW-11/LiF/Ag	6.2	-	22,800	52
2017.06	ITO/PFN-OX/Perovskite/TAPC/MoO ₃ /Au	0.016	-	560	53
2017.07	AnoHIL/Perovskite/TPBI/LiF/Al	8.66	-	~20,000	54
2017.07	ITO/PEDOT/Perovskite/TPBI/Ca/Ag	0.17	-	6,942	55
2017.11	ITO/P-NiO/Perovskite/TPBI/LiF/Al	4.36	-	6,530	56
2017.12	ITO/PEDOT/Perovskite/TPBI/LiF/Ag	-	0.95	1,784	57
2018.05	ITO/LiF/Perovskite/LiF/Bphen/LiF/Al	-	9.8	29,268	58
2018.10	ITO/Buf-HIL/Perovskite/TPBI/LiF/Al	0.86	-	604	59
2018.11	ITO/PSS-g-PANI/Perovskite/TPBI/LiF/Al	2.96	-	6145	60
2019.02	ITO/PEDOT/Di-NPB/Perovskite/Bmpyphb/LiF/Ag	-	7.0	6,600	61
2019.04	SOCP/Perovskite/TPBI/LiF/Al	11.7	-	~25,000	35
2019.04	ITO/PEDOT/Perovskite/BCP/LiF/Al	-	1.1	2,434	62
2019.06	ITO/PEDOT:PSS-Na/Perovskite/TPBI/LiF/Ag	1.44	-	13,883	63
2020.03	ITO/PEDOT/PVK/Perovskite/AgNWs	8.85	-	3,350	64
2020.06	FTO/Buf-HIL/Perovskite/TPBI/LiF/Al	4.23	-	~20,000	28
2020.08	ITO/PEDOT/Perovskite/TPBI/LiF/Ag	1.86	-	1,610	65
2021.11	ITO/PEDOT/Perovskite/TPBI/LiF/Al	10.3	-	~20,000	66
This work	CPA/Perovskite/TPBI/LiF/Al	14.16	67.32	15.381	-

Table 2-2. Bi-exponential decay function fitted results of PL lifetime curves of pristine and thiol-incorporated MAPbBr₃ films on glass/CPA substrates.

Film	τ_1 (ns)	f_1 (%)	τ_2 (ns)	f_2 (%)	τ_{ave} (ns)
CPA/pristine MAPbBr ₃	35.68	36.43	146.27	63.57	105.98

CPA/thiol-incorporated MAPbBr ₃	46.89	24.99	232.12	75.01	185.82
---	-------	-------	--------	-------	--------

Table 2-3. Device characteristics of PeLEDs using pristine or thiol-incorporated MAPbBr₃ based on different anode.

Anode	Perovskite	Luminance (cd m ⁻²)	Current efficiency (cd A ⁻¹)	EQE (%)
FTO	Polycrystalline MAPbBr ₃	14183	23.41	5.39
FTO	CSNP MAPbBr ₃	21757	39.11	7.87
CPA	Polycrystalline MAPbBr ₃	10130	40.67	8.69
CPA	CSNP MAPbBr ₃	15381	67.32	14.16

2.5. Bibliography

1. Quan, L. N. *et al.* Perovskites for Next-Generation Optical Sources. *Chemical Reviews* **119**, 7444–7477 (2019).
2. Xing, G. *et al.* Transcending the slow bimolecular recombination in lead-halide perovskites for electroluminescence. *Nature Communications* **8**, 14558 (2017).
3. D’Innocenzo, V. *et al.* Excitons versus free charges in organo-lead tri-halide perovskites. *Nature Communications* **5**, 3586 (2014).
4. He, H. *et al.* Exciton localization in solution-processed organolead trihalide perovskites. *Nature Communications* **7**, 10896 (2016).
5. Zhou, Q. *et al.* In Situ Fabrication of Halide Perovskite Nanocrystal-Embedded Polymer Composite Films with Enhanced Photoluminescence for Display Backlights. *Advanced Materials* **28**, 9163–9168 (2016).
6. Huang, H. *et al.* Top-Down Fabrication of Stable Methylammonium Lead Halide Perovskite Nanocrystals by Employing a Mixture of Ligands as Coordinating Solvents. *Angewandte Chemie* **129**, 9699–9704 (2017).
7. Huang, H., Bodnarchuk, M. I., Kershaw, S. V., Kovalenko, M. V. & Rogach, A. L. Lead Halide Perovskite Nanocrystals in the Research Spotlight: Stability and Defect Tolerance. *ACS Energy Letters* **2**, 2071–2083 (2017).
8. Kim, Y.-H. *et al.* Comprehensive defect suppression in perovskite nanocrystals for high-efficiency light-emitting diodes. *Nature Photonics* **15**, 148–155 (2021).
9. Jiang, Y. *et al.* Reducing the impact of Auger recombination in quasi-2D perovskite light-emitting diodes. *Nature Communications* **12**, 336 (2021).

10. Lin, K. *et al.* Perovskite light-emitting diodes with external quantum efficiency exceeding 20 per cent. *Nature* **562**, 245–248 (2018).
11. Fang, Z. *et al.* Dual Passivation of Perovskite Defects for Light-Emitting Diodes with External Quantum Efficiency Exceeding 20%. *Advanced Functional Materials* **30**, 1–9 (2020).
12. Chiba, T. *et al.* Anion-exchange red perovskite quantum dots with ammonium iodine salts for highly efficient light-emitting devices. *Nature Photonics* **12**, 681–687 (2018).
13. Hassan, Y. *et al.* Ligand-engineered bandgap stability in mixed-halide perovskite LEDs. *Nature* **591**, 72–77 (2021).
14. Zhao, B. *et al.* High-efficiency perovskite-polymer bulk heterostructure light-emitting diodes. *Nature Photonics* vol. 12 783–789 Preprint at <https://doi.org/10.1038/s41566-018-0283-4> (2018).
15. Vasilopoulou, M. *et al.* Advances in solution-processed near-infrared light-emitting diodes. *Nature Photonics* **15**, 656–669 (2021).
16. Zhao, X. & Tan, Z.-K. Large-area near-infrared perovskite light-emitting diodes. *Nature Photonics* **14**, 215–218 (2020).
17. Cao, Y. *et al.* Perovskite light-emitting diodes based on spontaneously formed submicrometre-scale structures. *Nature* **562**, 249–253 (2018).
18. Cho, H. *et al.* Overcoming the electroluminescence efficiency limitations of perovskite light-emitting diodes. *Science (2015)* **350**, 1222–1225.
19. Ono, L. K., Liu, S. & Qi, Y. Reducing Detrimental Defects for High-Performance Metal Halide Perovskite Solar Cells. *Angewandte Chemie – International Edition* **59**, 6676–6698 (2020).

20. Zhou, Y., Poli, I., Meggiolaro, D., De Angelis, F. & Petrozza, A. Defect activity in metal halide perovskites with wide and narrow bandgap. *Nature Reviews Materials* **0123456789**, (2021).
21. Woo, S. J., Kim, J. S. & Lee, T. W. Characterization of stability and challenges to improve lifetime in perovskite LEDs. *Nature Photonics* **15**, 630–634 (2021).
22. Park, M.-H. *et al.* Boosting Efficiency in Polycrystalline Metal Halide Perovskite Light-Emitting Diodes. *ACS Energy Letters* **4**, 1134–1149 (2019).
23. Chen, B., Rudd, P. N., Yang, S., Yuan, Y. & Huang, J. Imperfections and their passivation in halide perovskite solar cells. *Chemical Society Reviews* **48**, 3842–3867 (2019).
24. Lai, M. *et al.* Intrinsic anion diffusivity in lead halide perovskites is facilitated by a soft lattice. *Proceedings of the National Academy of Sciences* **115**, 11929–11934 (2018).
25. Yuan, Y. & Huang, J. Ion Migration in Organometal Trihalide Perovskite and Its Impact on Photovoltaic Efficiency and Stability. *Accounts of Chemical Research* **49**, 286–293 (2016).
26. Eames, C. *et al.* Ionic transport in hybrid lead iodide perovskite solar cells. *Nature Communications* **6**, 7497 (2015).
27. Kim, H. *et al.* Proton-transfer-induced 3D/2D hybrid perovskites suppress ion migration and reduce luminance overshoot. *Nature Communications* **11**, 3378 (2020).
28. Kim, H. *et al.* Proton-transfer-induced 3D/2D hybrid perovskites suppress ion migration and reduce luminance overshoot. *Nature Communications* **11**, 3378 (2020).

29. Chu, Z. *et al.* Perovskite Light-Emitting Diodes with External Quantum Efficiency Exceeding 22% via Small-Molecule Passivation. *Advanced Materials* **33**, 1–9 (2021).
30. Liang, A. *et al.* Highly Efficient Halide Perovskite Light-Emitting Diodes via Molecular Passivation. *Angewandte Chemie – International Edition* **60**, 8337–8343 (2021).
31. Ono, L. K., Liu, S. & Qi, Y. Reducing Detrimental Defects for High-Performance Metal Halide Perovskite Solar Cells. *Angewandte Chemie – International Edition* **59**, 6676–6698 (2020).
32. Noel, N. K. *et al.* Enhanced Photoluminescence and Solar Cell Performance via Lewis Base Passivation of Organic–Inorganic Lead Halide Perovskites. *ACS Nano* **8**, 9815–9821 (2014).
33. Yang, X. *et al.* Efficient green light-emitting diodes based on quasi-two-dimensional composition and phase engineered perovskite with surface passivation. *Nature Communications* **9**, 2–9 (2018).
34. Sutanto, A. A. *et al.* Phosphine Oxide Derivative as a Passivating Agent to Enhance the Performance of Perovskite Solar Cells. *ACS Applied Energy Materials* **4**, 1259–1268 (2021).
35. Park, M. *et al.* Efficient Perovskite Light-Emitting Diodes Using Polycrystalline Core–Shell-Mimicked Nanograins. *Advanced Functional Materials* **29**, 1902017 (2019).
36. Kim, Y.-H. *et al.* Multicolored Organic/Inorganic Hybrid Perovskite Light-Emitting Diodes. *Advanced Materials* **27**, 1248–1254 (2015).
37. Cho, H. *et al.* Overcoming the electroluminescence efficiency limitations of

- perovskite light-emitting diodes. *Science (1979)* **350**, 1222–1225 (2015).
38. Jeong, S.-H. *et al.* Characterizing the Efficiency of Perovskite Solar Cells and Light-Emitting Diodes. *Joule* **4**, 1206–1235 (2020).
39. Van Gompel, W. T. M. *et al.* Degradation of the Formamidinium Cation and the Quantification of the Formamidinium–Methylammonium Ratio in Lead Iodide Hybrid Perovskites by Nuclear Magnetic Resonance Spectroscopy. *Journal of Physical Chemistry C* **122**, 4117–4124 (2018).
40. Park, M. H. *et al.* Unravelling additive-based nanocrystal pinning for high efficiency organic–inorganic halide perovskite light-emitting diodes. *Nano Energy* **42**, 157–165 (2017).
41. Kim, Y. H. *et al.* High efficiency perovskite light-emitting diodes of ligand-engineered colloidal formamidinium lead bromide nanoparticles. *Nano Energy* **38**, 51–58 (2017).
42. He, J. *et al.* Surface chelation of cesium halide perovskite by dithiocarbamate for efficient and stable solar cells. *Nature Communications* **11**, 1–8 (2020).
43. Du, P. *et al.* Efficient and large-area all vacuum-deposited perovskite light-emitting diodes via spatial confinement. *Nature Communications* **12**, 1–10 (2021).
44. Xing, G. *et al.* Solution-Processed Tin-Based Perovskite for Near-Infrared Lasing. *Advanced Materials* **28**, 8191–8196 (2016).
45. Schmidt, T., Lischka, K. & Zulehner, W. Excitation–power dependence of the near-band-edge photoluminescence of semiconductors. *Physical Review B* **45**, 8989–8994 (1992).
46. Gershon, T. *et al.* Photoluminescence characterization of a high-efficiency Cu

- 2ZnSnS₄ device. *Journal of Applied Physics* **114**, (2013).
47. Ling, Y. *et al.* Bright Light-Emitting Diodes Based on Organometal Halide Perovskite Nanoplatelets. *Advanced Materials* **28**, 305–311 (2016).
 48. Shi, Z. F. *et al.* High-performance planar green light-emitting diodes based on a PEDOT:PSS/CH₃NH₃PbBr₃/ZnO sandwich structure. *Nanoscale* **8**, 10035–10042 (2016).
 49. Wang, Z., Cheng, T., Wang, F., Dai, S. & Tan, Z. Morphology Engineering for High-Performance and Multicolored Perovskite Light-Emitting Diodes with Simple Device Structures. *Small* **12**, 4412–4420 (2016).
 50. Seo, H.-K. *et al.* Efficient Flexible Organic/Inorganic Hybrid Perovskite Light-Emitting Diodes Based on Graphene Anode. *Advanced Materials* **29**, 1605587 (2017).
 51. Lee, J.-W. *et al.* In-Situ Formed Type I Nanocrystalline Perovskite Film for Highly Efficient Light-Emitting Diode. *ACS Nano* **11**, 3311–3319 (2017).
 52. Lee, S. *et al.* Amine-Based Passivating Materials for Enhanced Optical Properties and Performance of Organic-Inorganic Perovskites in Light-Emitting Diodes. *The Journal of Physical Chemistry Letters* **8**, 1784–1792 (2017).
 53. Leyden, M. R. *et al.* Methylammonium Lead Bromide Perovskite Light-Emitting Diodes by Chemical Vapor Deposition. *The Journal of Physical Chemistry Letters* **8**, 3193–3198 (2017).
 54. Jeong, S.-H. *et al.* Universal high work function flexible anode for simplified ITO-free organic and perovskite light-emitting diodes with ultra-high efficiency. *NPG Asia Materials* **9**, e411–e411 (2017).

55. Li, J. *et al.* Sodium bromide additive improved film morphology and performance in perovskite light-emitting diodes. *Applied Physics Letters* **111**, 053301 (2017).
56. Ji, H. *et al.* Vapor-Assisted Solution Approach for High-Quality Perovskite CH₃NH₃PbBr₃ Thin Films for High-Performance Green Light-Emitting Diode Applications. *ACS Applied Materials & Interfaces* **9**, 42893–42904 (2017).
57. Kim, S. J. *et al.* Perovskite Light-Emitting Diodes via Laser Crystallization: Systematic Investigation on Grain Size Effects for Device Performance. *ACS Applied Materials & Interfaces* **10**, 2490–2495 (2018).
58. Zhang, M. *et al.* High performance organo-lead halide perovskite light-emitting diodes via surface passivation of phenethylamine. *Organic Electronics* **60**, 57–63 (2018).
59. Kim, J. S. *et al.* Increased luminescent efficiency of perovskite light emitting diodes based on modified two-step deposition method providing gradient concentration. *APL Materials* **6**, 111101 (2018).
60. Ahn, S. *et al.* Fine Control of Perovskite Crystallization and Reducing Luminescence Quenching Using Self-Doped Polyaniline Hole Injection Layer for Efficient Perovskite Light-Emitting Diodes. *Advanced Functional Materials* **29**, 1807535 (2019).
61. Prakasam, V. *et al.* Large area perovskite light-emitting diodes by gas-assisted crystallization. *Journal of Materials Chemistry C* **7**, 3795–3801 (2019).
62. Jung, D. H. *et al.* Flash-induced ultrafast recrystallization of perovskite for

- flexible light-emitting diodes. *Nano Energy* **61**, 236–244 (2019).
63. Xu, L. *et al.* Towards green antisolvent for efficient CH₃NH₃PbBr₃ perovskite light emitting diodes: A comparison of toluene, chlorobenzene, and ethyl acetate. *Applied Physics Letters* **115**, 033101 (2019).
64. An, H. J., Kim, Y. C., Kim, D. H. & Myoung, J.-M. High-Performance Green Light-Emitting Diodes Based on MAPbBr₃ with π -Conjugated Ligand. *ACS Applied Materials & Interfaces* **12**, 16726–16735 (2020).
65. Chang, S.-J., Li, L.-C., Hong, T.-H., Shellaiah, M. & Sun, K. W. Fabrication of centimeter-scale MAPbBr₃ light-emitting device with high color purity. *Organic Electronics* **86**, 105931 (2020).
66. Weng, S. *et al.* Light extraction efficiency enhancement of CH₃NH₃PbBr₃ light-emitting diodes using nanopatterned PEDOT:PSS layers. *Applied Physics Letters* **119**, 233302 (2021).

Chapter 3. Ideal Mixed-Cation System for Highly Efficient and Stable Perovskite Light-Emitting Diodes

3.1. Introduction

Metal halide perovskites (MHPs) are considered future emitting materials because of their extraordinary characteristics: low-cost material, color tunability, narrow emission spectra (full-width at half maximum (FWHM) ≈ 20 nm), and easy processability¹⁻⁵. Researcher have been studied for the achieving highly efficient perovskite light-emitting diodes (PeLEDs). Several strategies are chosen for the achievement (e.g., cation alloying for strong carrier confinements, polycrystalline defect passivation technique, small organic molecule additive, polymer additive, dimension control, and core/shell structure with organic ligand)^{3,5-11}. However, there is obstacle of charge transport and carrier confinement in both nanocrystal and bulk poly crystalline.¹²⁻¹⁸ Especially, the defect sites inside the polycrystalline perovskites can facilitate ion migration toward grain boundaries, then, destroying the crystal structure.¹⁹⁻²¹. Therefore, strategies to make ideal crystal structure for suppressing defect inside perovskite crystal should be developed for achieving high efficiency LEDs.

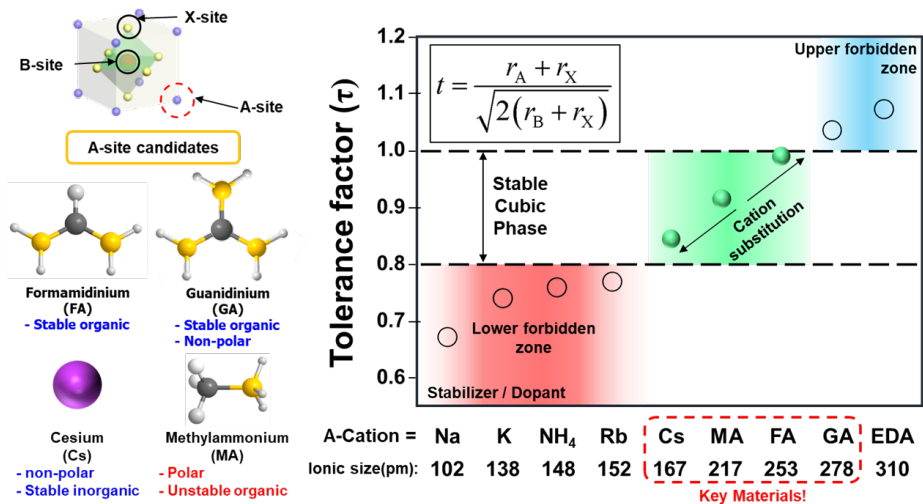


Figure 3-1. Illustration of candidate of cation for ideal mixed cation system.

Here, we introduce the quadruple cation perovskite structure for defect passivation of 3D polycrystalline perovskite. Most of mixed-cation system comes from these four cation in **Figure 3-1**. As mention in chapter one, tolerance factor should be located between 0.8 and 1.0 for stable perovskite structure. Therefore, we should consider the ionic radius of A-site cation for ideal mixed cation system.

Firstly, the unstable nature linked to small organic cation part (Methylammonium, MA) of perovskite crystals is studied in previously in our lab.^{5,22} We need developing a new MHP materials based on stable organic/inorganic hybrid mixed-cation system. With structurally and optically stable characteristics of mixed-cation system, we could fabricate highly efficient perovskite light-emitting diodes (PeLEDs) with enhanced device operation lifetime. To realize new MHP system with substitution of small MA cation which is mainly responsible to the degradation of MHP crystals, new stable cation site were selected; inorganic Cesium (Cs), large organic Formamidinium (FA), and zero-dipole organic Guanidinium (GA) cations. Compared with MA cation, these new candidates have potential to have much higher

thermal stability and moisture stability. Previously, we already introduce FA-Cs mixed cation system for stable and efficient PeLEDs (**Figure 3-2**)

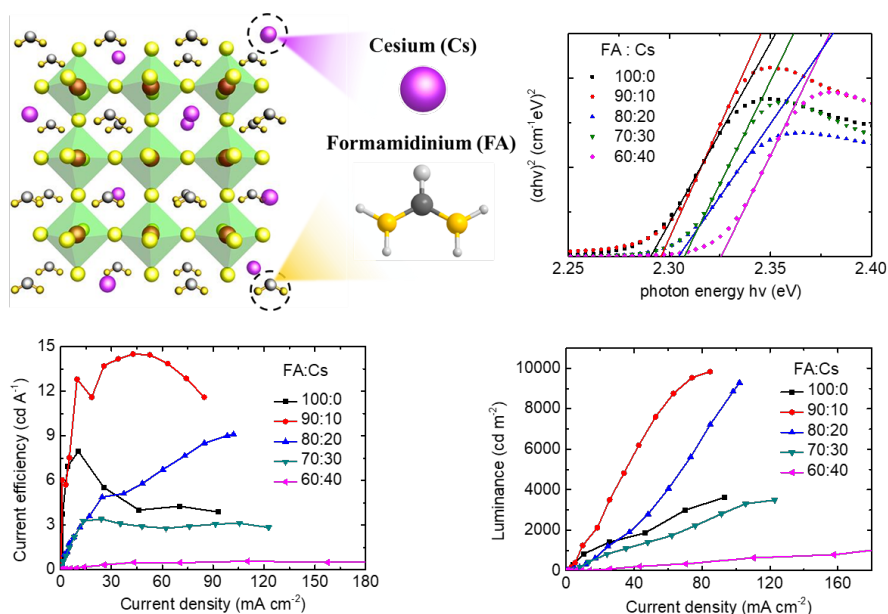


Figure 3-2. Role of Cs : FA-Cs Mixed cation for PeLEDs.

Stable Cs cation in the FA cation site can make the stable perovskite structure, and single-phase perovskite structure is earned by precise ratio control. Also, increased photo-stability can be attributed to much stable crystal structure and environmental stability of FA and Cs cations compared with MA cation, resulting in much higher tolerance to photo-induced excited state and photo-induced degradation during the measurement. It can be understood that the crystals under unstable intermediate state during irradiation could return to initial stable state with incorporation of stable cation such as Cs.

Furthermore, before we construct mixed-cation system using GA cation having zero dipole moment, properties of GA cation are briefly mentioned here. In previous paper in our lab,²³ GA (278 ppm), which has a larger ionic radius than FA (253 ppm) and Cs (181 ppm), forms a uniformly mixed alloy crystal with FA-based

perovskite nanocrystals. Unlike other cations, GA cation with three-handed hydrogen bonding sites with zero dipole moment could minimize the fluctuation of soft ionic lattice and prevents local defect formation, improving the luminescence properties of perovskite crystals (**Figure 3-3**).

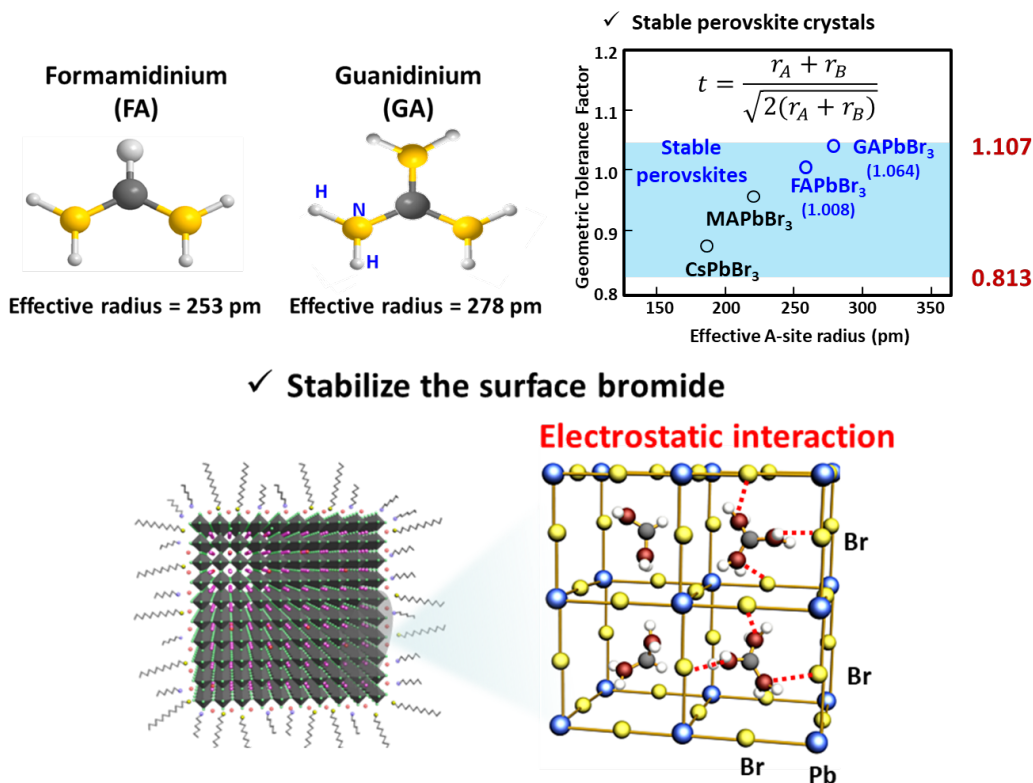


Figure 3-3. Advantage of Guanidium cation for FA-based perovskite structure.

In the quadruple-cation perovskite nanoparticles in which defects were passivated, the trap density was greatly decreased, and the radiative recombination efficiency was significantly increased by ~300 times compared to the polycrystalline 3D perovskites. PeLEDs based on quadruple-cation structure showed maximum current efficiency of 151 cd A⁻¹ (maximum EQE of 28.9%), maximum brightness of ~470,000 cd m⁻², very little efficiency roll-off (~5% even at 300,000 cd m⁻²) and very long estimated half-lifetime of >14h at 100,00 cd m⁻² with green emission at EL

peak of 540 nm, showing excellent performance in all aspects of efficiency, luminance, and lifetime simultaneously.

3.2. Materials and Experiments

Materials. Formamidinium bromide (FABr, > 99.99%), Methylammonium bromide (MABr, > 99.99%), and were purchased from Dyesol. Guanidinium bromide (GABr, > 98%) Cesium bromide (CsBr), BPA, tetrafluoroethylene-perfluoro3,6-dioxo-4-methyl-7-octene-sulfonic acid copolymer (PFI), Chlorobenzene (CB), Tetrahydrofuran (THF), and Molybdenum oxide (MoO_3) were purchased from Sigma-Aldrich. Lead bromide (PbBr_2) was purchased from TCI. 2,2',2''-(1,3,5-Benzinetriyl)-tris(1-phenyl-1H-benzimidazole) (TPBi) was purchased from OSM. 9,10-di(naphthalene-2-yl)anthracen-2-yl-(4,1-phenylene)(1-phenyl-1H-benzo[d]imidazole) (ZADN) was purchased from Shinwon Chemtrade. Lithium fluoride (LiF) was purchased from Foosung. Unless otherwise stated, all materials are used without purification.

Preparation of MHP solution. The ideal mixed-cation precursor, $((\text{FA}_{0.7}\text{MA}_{0.1}\text{GA}_{0.2})_{0.87}\text{Cs}_{0.13}\text{PbBr}_3)$ was prepared by dissolving FABr, MABr, GABr, CsBr and PbBr_2 (molar ratio of $(\text{FABr} + \text{MABr} + \text{GABr} + \text{CsBr}) : \text{PbBr}_2 = 1.15 : 1$) in $\text{DMSO}^{9,24}$. Also, we added 5 mol % of BPA relative to PbBr_2 . The solution was stirred overnight in N_2 -filled glove box before use.

Fabrication of perovskite film and PeLEDs. Pre-patterned (Half pattern) FTO(300nm) glasses (25 mm X 25 mm) were sonicated in acetone and 2-propanol for 15 min each sequentially, then boiled in 2-propanol for 30 min. UVO treatment are done for the hydrophilic surface of substrate(FTO, glass, and Si-wafer. It depends on the experiment). We used a previously-described method⁴ to synthesize a Hole

injection layer called Buf-HIL that has a gradient work function (WF), by inducing self-organization of PEDOT:PSS (CLEVIOS P VP AI4083) and tetrafluoroethylene-perfluoro3,6-dioxa-4-methyl-7-octene-sulfonic acid copolymer (PFI); the solution was spin-coated to form 70-nm thickness, then annealed at 150 °C for 30 min⁴. After baking, the substrates were transferred into a N₂-filled glove box for deposition of perovskite layer. MHP films were deposited by spin-coating the precursor solution at 6000 rpm with additive-assisted nanocrystal pinning (A-NCP) process:²⁵ during the second spin step, TPBi-dissolved CB solution was dropped onto the spinning perovskite film. And then, BPA dissolved in THF solution was loaded on top of the perovskite, followed by reaction time of 30s and direct spin-drying afterward for making the defect passivation effect. The prepared perovskite films were baked on a hotplate at 70 °C for 10 min. Samples were moved to the high vacuum chamber (<10⁻⁷ Torr) through N-filled glovebox to sequentially deposit ZADN (45 nm), LiF (1.2 nm), and Al (100 nm). Finally, the fabricated PeLEDs were encapsulated under N₂ atmosphere by using a glass lid and UV-curable epoxy resin.

Perovskite film characterizations. The X-ray diffraction (XRD) measurement was performed using an X-ray diffractometer (BRUKER MILLER Co., D8-Advance) with Cu K α radiation ($\lambda = 1.54056 \text{ \AA}$). XRD data were gained in the 2θ range of 10°-50° at room temperature. Top-view and cross-sectional scanning electron microscopy (SEM) images of Si wafer/GraHIL/ perovskite films were measured using a field-emission scanning electron microscope (FESEM) (SUPRA 55VP) at the NICEM. Steady-state photoluminescence (PL) spectra and

ultraviolet/visible (UV-Vis) absorption spectra were measured by using a JASCO FP8500 spectrofluorometer and Lambda-465 UV-Vis spectrophotometer. For PL and UV-vis measurement, perovskite films are encapsulated under N₂ atmosphere with same. Methods above. Xenon arc lamp with continuous-output power of 150 W was used as an excitation source, and the excitation wavelength was 405 nm (could be controlled). The light was incident toward the glass side that is opposite to the perovskite film/N₂ interface. To measure PL lifetime, a photon-counting detector (PMA Hybrid 07) and time-correlated single-photon counting (TCSPC) module (PicoHarp, PicoQuant) were used. Instrument response function (IRF) was ignored because the PL lifetime curves were much longer than the temporal width of the IRF. The excitation power density was $\sim 25 \text{ mW cm}^{-2}$, and the excitation wavelength was fixed at 405 nm. For single-carrier device analysis, MoO₃ (30nm) and Au (50nm) were thermally deposited sequentially onto ITO/GraHIL/perovskite and encapsulated in N₂ atmosphere to obtain the current-voltage curve using a Keithley 236 source measurement unit.

Performance evaluation of perovskite LEDs. Electroluminescence efficiencies of the fabricated PeLEDs were measured using a Keithley 236 source measurement unit and a Minolta CS-2000 spectroradiometer. External quantum efficiency of PeLEDs was calculated by measuring same with previous paper²⁶. Operational lifetime of

PeLEDs was measured under constant current condition by a M760 Lifetime Analyzer (Mscience Inc.).

3.3. Results and Discussion

We systematically analyze the structure and optical properties of the perovskite structure by partially substituting GA cation into the existing FA-Cs double-cation system. As the proportion of substituted GA concentration increases, forms a uniformly mixed alloy crystal, which is known as peak shift on X-ray diffraction (XRD). Constant increase was seen. (Figure 3-4).

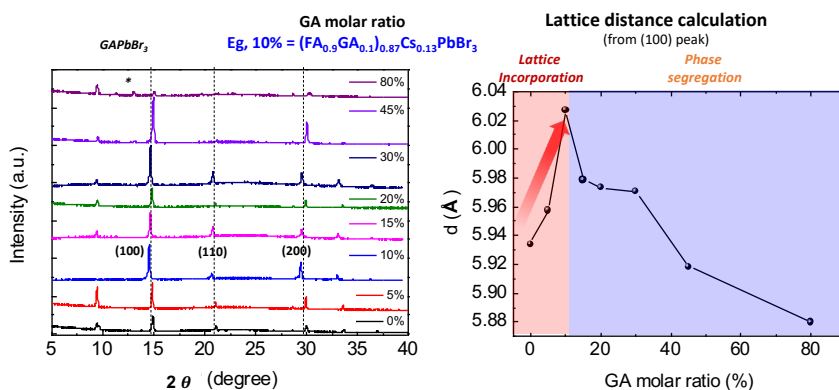


Figure 3-4. Structural analysis with changing GA cation ratio in FA-Cs system.

The lattice constant increased linearly as the molar ratio of GA increased from 0% ($a = 5.93\text{\AA}$) to 10% ($a = 6.03\text{\AA}$), and higher molar ratio reduced lattice constant continuously. This result shows the GA is located at the FA-cation site until 10 mol % ratio that are same with previous results.²³ when the lots of GA cation substitution are occurs, GAPbBr₃ phase is earned which is 0D perovskite, so lots of GA cation make phase segregation. We also see the phase segregation in SEM image in Figure 3-5. Interestingly, there is XRD peak in 9 are shown which comes from the FA₂PbBr₄ structure (Figure 3-6). We also using stoichiometric control methods for the efficient PeLEDs.^{5,21,22} This stoichiometric control increases the possibility of formation of

FA₂PbBr₄ phase. Therefore, larger GA cation make the difference UV-vis spectrum change.²⁷

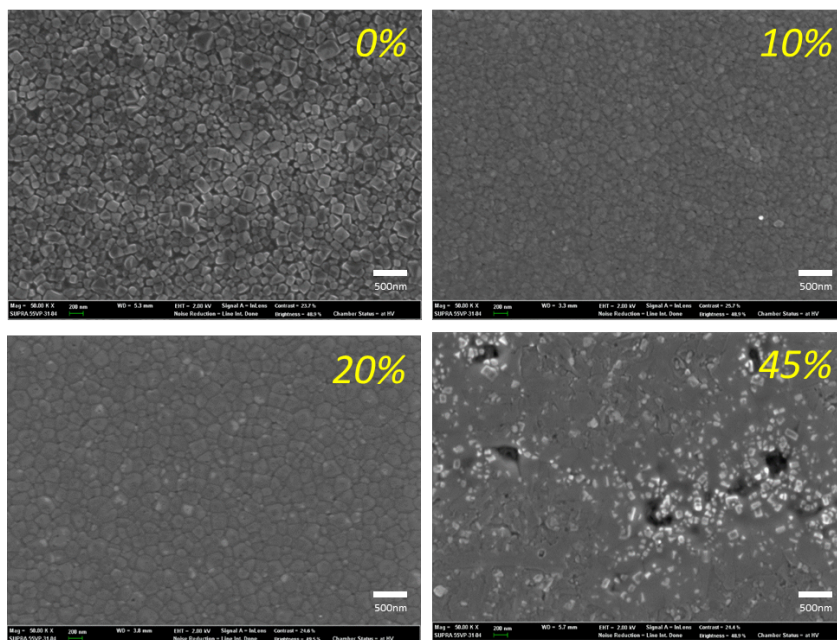


Figure 3-5. SEM analysis with different GA cation ratio (yellow mark are GA substitution ratio in FA-site).

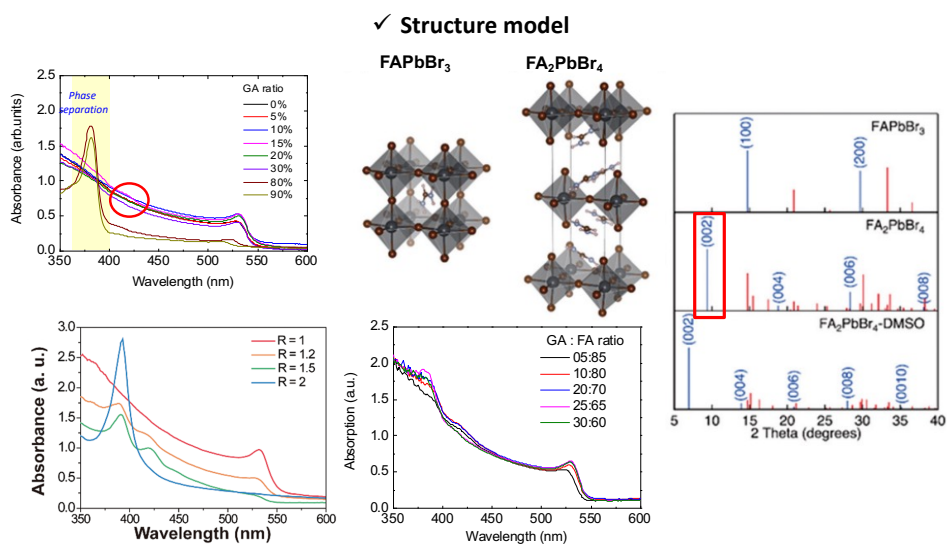


Figure 3-6. UV-vis Absorption spectrum and structure model for FAPbBr₃ and FA₂PbBr₄, absorption of stoichiometric control with FAPbBr₃: PbBr₂ ratio Copyright 2019, Royal Society of Chemistry.²⁷

Also, the PL intensity of 30% GA incorporated films showed increased PL intensity by about 13 times compared with double-cation system, and the PL lifetime was also increased 3-fold. The result indicates that the luminescence properties could be improved due to the formation of a more stable crystal structure in triple-cation system (**Figure 3-7**). Furthermore, PL and UV-vis spectra also show the phase segregation results with large amount of GA cooperation.

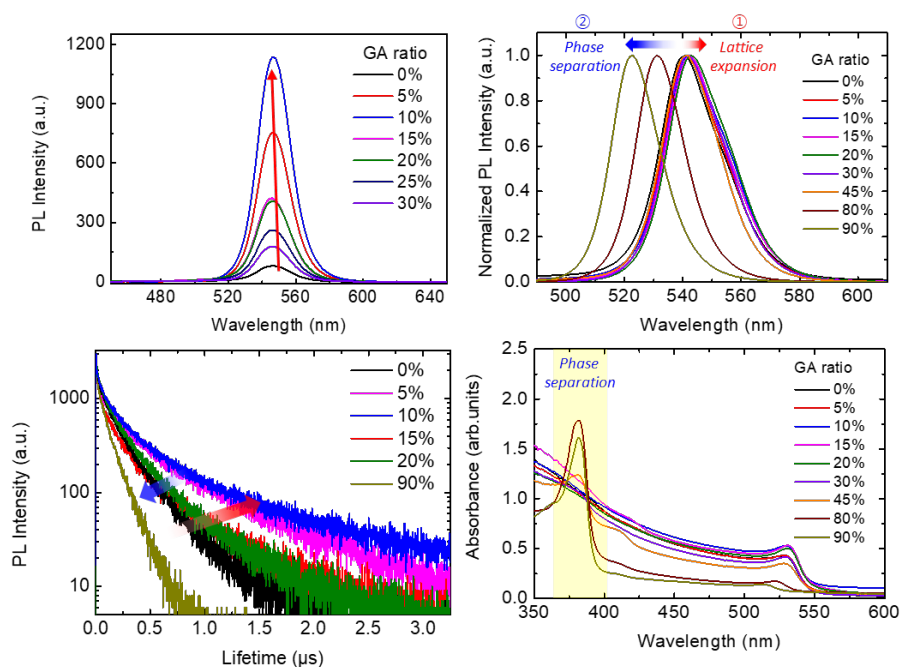


Figure 3-7. Optoelectronic properties with changing GA cation ratio in FA-Cs system

We also made the PeLEDs using the conventional OLED structure. This triple-cation system with different ratio of GA cation ratio shows the similar tendencies. (**Figure 3-8 and table 3-1**) almost six times enhancement of efficiency (16.42 cd A^{-1} to 97.39 cd A^{-1}) increasement are shown with GA substitution, which are same reason of the other result. Also, luminance properties of device are significantly increased. Defect passivation of GA cation are main reason for this outstanding device performance.

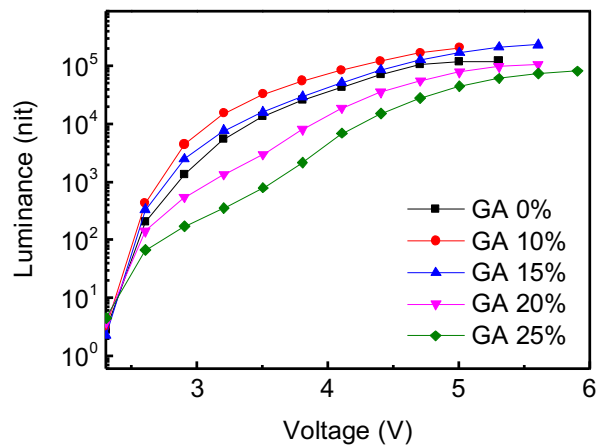
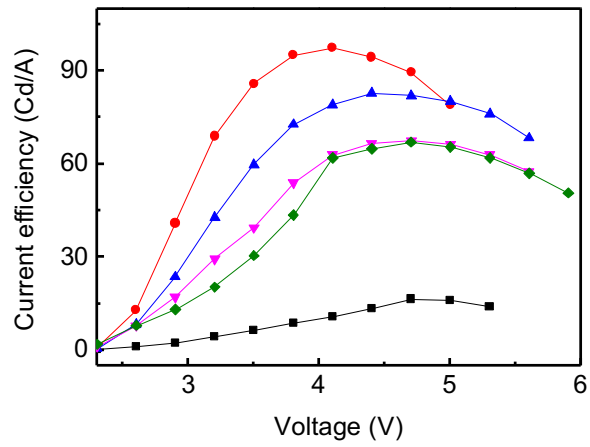
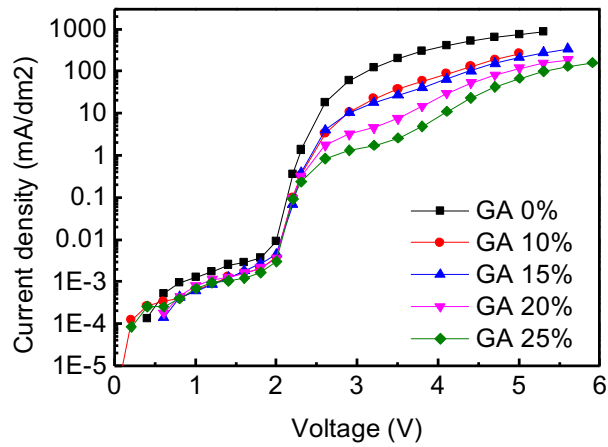


Figure 3-8. J-V-L Characteristics with changing GA cation in FA-CS system.

As mentioned above, defect passivation are the main reason of this increment of device results. So, we made the single-carrier device (hole-only device) for the calculate the trap density (**Figure 3-9 and table 3-2**). Trap filled limit voltage are decreased (0.312 V to 0.193 V), so trap density are decreased with GA cation substitution.

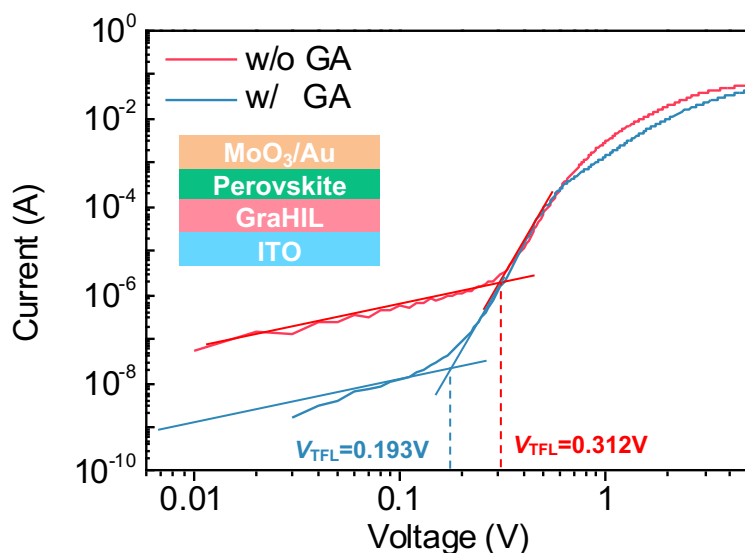


Figure 3-9. hole-only device results comparison between w/o GA and w/ GA

The GA is attractive cation for passivate the defects, but there is limitation of substitution ratio because of large ionic radius and tolerance factor (**Figure 3-1**). Therefore, we introduced the MA cation as a counterpart of GA cation for the triple cation (FA-GA-Cs) system. We firstly analyze the PL intensity change with varying MA and GA cation ratio (**Figure 3-10**). Before we analyze the PL characteristics, tolerance factor was calculated for knowing possibility of structure formation of quadruple cation system. As you see, more MA cation are added, we could substitute the more GA cation, because small MA cations act as a counterpart of GA cation.

Same with this assumption, PL intensity are increased with larger GA ratio. Finally, we could unique ratio of quadruple system: $(\text{FA}_{0.7}\text{GA}_{0.2}\text{MA}_{0.1})_{0.87}\text{CS}_{0.13}$. We could see PL intensity is continuously increased from double to quadruple cation system. Too many GA could make the phase segregation as mentioned above (**Figure 3-5**). We could maximize the advantage of GA cation using this unique ratio of mixed cation system.

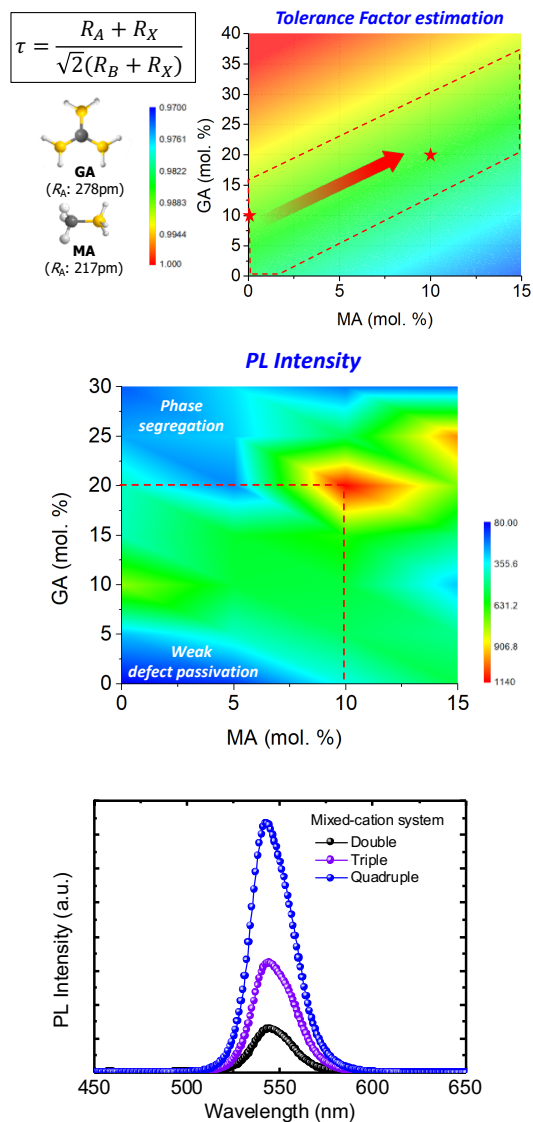


Figure 3-10. Tolerance factor and PL Intensity changes with MA & GA ratio.

We also made the PeLEDs based on these properties to comparing different mixed-cation system (**Figure 3-11 and table 3-3**). Also, PeLEDs based on quadruple cation with precisely controlled composite result in excellent device efficiency with maximum brightness (L_{\max}) $> 470,000\text{cd m}^{-2}$ and maximum external quantum efficiency (EQE^{\max}) $\geq 29.84\%$. Especially, this ideal mixed cation system have high reproducibility (**Figure 3-12**). In particular, the maximum brightness of $> 470,000\text{cd m}^{-2}$ is to our knowledge the highest brightness value among PeLEDs reported to date, showing the possibility of high-brightness applications and stable operation in outdoor lighting. Also, PeLEDs characteristics of triple cation system without GA cation (FA-MA-Cs) poor device performance, thus GA cation are play a key role in the mixed cation system, and MA are used just for substituting more GA in FA-site. Further, unlike the conventional double-cation or triple cation system PeLEDs with very low operation lifetime of $< 1\text{hr}$ at initial brightness of $100,00\text{ cd m}^{-2}$, the quadruple-cation system showed half-lifetime of $\sim 14\text{hr}$. The result indicates that the ideal mixed-cation system can stabilize the crystal structure and passivate the defect states, improving the operational stability as well.

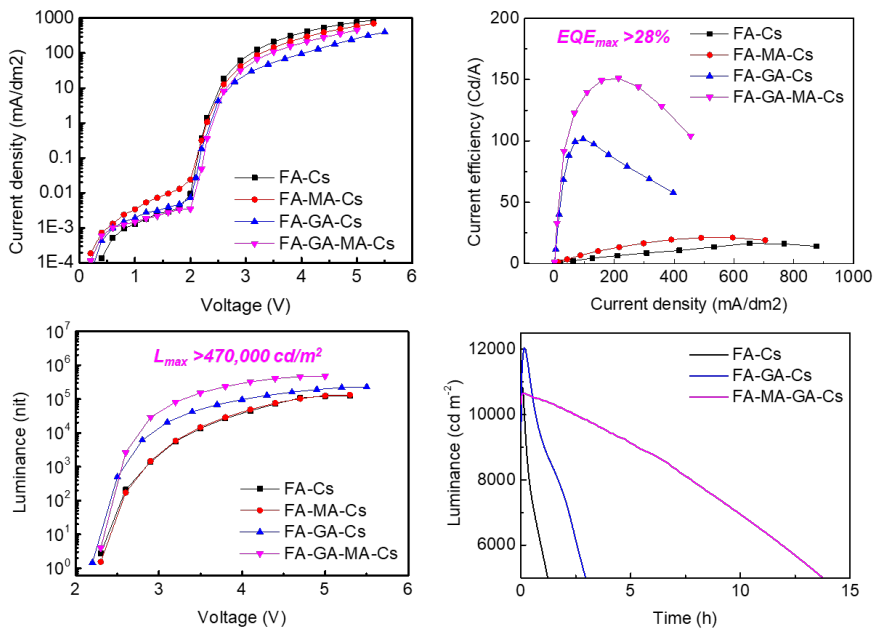


Figure 3-11. J-V-L Characteristics and lifetime analysis with different mixed cation system perovskite (e.g.; FA-Cs, FA-GA-Cs, FA-MA-GA-Cs)

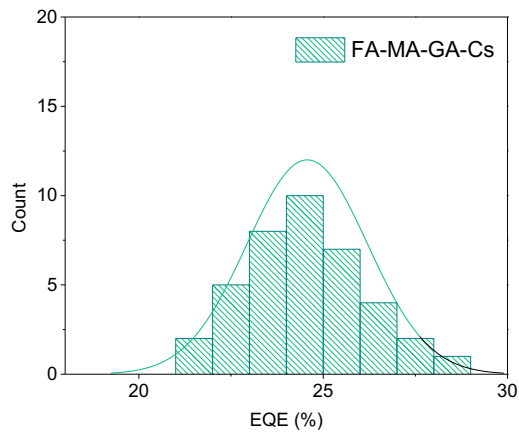


Figure 3-10. Histogram of EQE with quadruple cation PeLEDs

3.4. Conclusion

In summary, we demonstrated quadruple-cation structured perovskite with polycrystalline quadruple-cation perovskite thin films. This quadruple-cation structure enabled increased carrier confinement, reduction in trap density, and increase in luminous efficiency without sacrificing the charge transport properties of 3D perovskites. Especially, we choose the GA as an new A-site cation for ideal mixed-cation system. Firstly, substitution ratio of GA cation is only 10 mol% because of large ionic radius characteristics. So, we introduced the MA as an counterpart cation to substitute more GA in FA-site. We could substitute the GA cation 20 mol% in FA-site by this ideal quadruple cation system. We could maximize the advantage of GA cation, and effectively passivate the defect state of 3D perovskite. As a result, simultaneously ultra-bright, efficient and stable PeLEDs with maximum current efficiency of 151 cd A^{-1} (maximum EQE of 28.9%), maximum luminance of $\sim 470,000 \text{ cd m}^{-2}$, and lifetime are measured with T_{50} of 14h ($L_0=100,000 \text{ cd m}^{-2}$) were demonstrated. These results suggest that PeLEDs are not only laboratory-level high-efficiency devices, but also a promising candidate for display and lighting applications for commercial displays.

Table 3-1. Table of CE, EQE, Luminance PeLEDs characteristics with different GA ratio.

GA mol. %	0	10	15	20	25
Max. CE [cd A-1]	16.42	97.39	82.83	67.58	67.03
Max. L [cd m-2]	122.789	210,890	237,406	109,711	83.438
Max. EQE [%]	3.67	19.30	16.99	14.05	14.59

Table 3-2 single-carrier device results for the trap density calculation both w/ GA cation and w/o GA

	w/o GA	w/ GA
Trap-filled-limit voltage, V_{TFL} [V]	0.312	0.193
Trap density, N_t [cm ⁻³]	1.89×10^{16}	1.17×10^{16}

Table 3-3 Table of CE, EQE, Luminance PeLEDs characteristics with different mixed cation system.

GA mol. %	FA-Cs	FA-GA-Cs	FA-MA-GA-Cs
Max. CE [cd A⁻¹]	16.4	97.39	151.1
Max. L [cd m⁻²]	122.789	210,890	473,990
Max. EQE [%]	3.67	19.30	28.94
Lifetime 10,000nit [h]	1.2	3.0	13.8

3.5. Bibliography

1. Tan, Z.-K. *et al.* Bright light-emitting diodes based on organometal halide perovskite. *Nature Nanotechnology* **9**, 687–692 (2014).
2. Kim, Y.-H., Cho, H. & Lee, T.-W. Metal halide perovskite light emitters. *Proc Natl Acad Sci U S A* **113**, 11694–11702 (2016).
3. Yuan, M. *et al.* Perovskite energy funnels for efficient light-emitting diodes. *Nature Nanotechnology* **11**, 872–879 (2016).
4. Kim, Y.-H. *et al.* Multicolored Organic/Inorganic Hybrid Perovskite Light-Emitting Diodes. *Advanced Materials* **27**, 1248–1254 (2015).
5. Cho, H. *et al.* Overcoming the electroluminescence efficiency limitations of perovskite light-emitting diodes. *Science (1979)* **350**, 1222–1225 (2015).
6. Lin, K. *et al.* Perovskite light-emitting diodes with external quantum efficiency exceeding 20 per cent. *Nature* **562**, 245–248 (2018).
7. Yang, X. *et al.* Efficient green light-emitting diodes based on quasi-two-dimensional composition and phase engineered perovskite with surface passivation. *Nature Communications* **9**, 2–9 (2018).
8. Zhao, B. *et al.* High-efficiency perovskite-polymer bulk heterostructure light-emitting diodes. *Nature Photonics* **12**, 783–789 (2018).
9. Kim, Y.-H. *et al.* Comprehensive defect suppression in perovskite nanocrystals for high-efficiency light-emitting diodes. *Nature Photonics* **15**, 148–155 (2021).
10. Kim, Y.-H., Kim, J. S. & Lee, T. Strategies to Improve Luminescence Efficiency of Metal-Halide Perovskites and Light-Emitting Diodes. *Advanced Materials* **31**, 1804595 (2019).

11. Park, M.-H. *et al.* Boosting Efficiency in Polycrystalline Metal Halide Perovskite Light-Emitting Diodes. *ACS Energy Letters* **4**, 1134–1149 (2019).
12. Wehrenfennig, C., Eperon, G. E., Johnston, M. B., Snaith, H. J. & Herz, L. M. High Charge Carrier Mobilities and Lifetimes in Organolead Trihalide Perovskites. *Advanced Materials* **26**, 1584–1589 (2014).
13. Herz, L. M. Charge-Carrier Mobilities in Metal Halide Perovskites: Fundamental Mechanisms and Limits. *ACS Energy Letters* **2**, 1539–1548 (2017).
14. Xu, W. *et al.* Rational molecular passivation for high-performance perovskite light-emitting diodes. *Nature Photonics* **13**, 418–424 (2019).
15. Meggiolaro, D., Mosconi, E. & De Angelis, F. Formation of Surface Defects Dominates Ion Migration in Lead-Halide Perovskites. *ACS Energy Letters* **4**, 779–785 (2019).
16. Cho, H., Kim, Y.-H., Wolf, C., Lee, H.-D. & Lee, T.-W. Improving the Stability of Metal Halide Perovskite Materials and Light-Emitting Diodes. *Advanced Materials* **30**, 1704587 (2018).
17. Liu, M., Matuhina, A., Zhang, H. & Vivo, P. Advances in the Stability of Halide Perovskite Nanocrystals. *Materials* **12**, 3733 (2019).
18. Dong, Y. *et al.* Bipolar-shell resurfacing for blue LEDs based on strongly confined perovskite quantum dots. *Nature Nanotechnology* **15**, 668–674 (2020).
19. Cho, H., Kim, Y.-H., Wolf, C., Lee, H.-D. & Lee, T.-W. Improving the Stability of Metal Halide Perovskite Materials and Light-Emitting Diodes. *Advanced Materials* **30**, 1704587 (2018).

20. Dong, Q., Lei, L., Mendes, J. & So, F. Operational stability of perovskite light emitting diodes. *Journal of Physics: Materials* **3**, 012002 (2020).
21. Kim, H. *et al.* Proton-transfer-induced 3D/2D hybrid perovskites suppress ion migration and reduce luminance overshoot. *Nature Communications* **11**, 3378 (2020).
22. Park, M. *et al.* Efficient Perovskite Light-Emitting Diodes Using Polycrystalline Core-Shell-Mimicked Nanograins. *Advanced Functional Materials* **29**, 1902017 (2019).
23. Kim, Y.-H. *et al.* Comprehensive defect suppression in perovskite nanocrystals for high-efficiency light-emitting diodes. *Nature Photonics* **15**, 148–155 (2021).
24. Cho, H. *et al.* High-Efficiency Polycrystalline Perovskite Light-Emitting Diodes Based on Mixed Cations. *ACS Nano* **12**, 2883–2892 (2018).
25. Cho, H. *et al.* Overcoming the electroluminescence efficiency limitations of perovskite light-emitting diodes. *Science (1979)* **350**, 1222–1225 (2015).
26. Jeong, S.-H. *et al.* Characterizing the Efficiency of Perovskite Solar Cells and Light-Emitting Diodes. *Joule* **4**, 1206–1235 (2020).
27. Shin, M. *et al.* Low-dimensional formamidinium lead perovskite architectures via controllable solvent intercalation. *Journal of Materials Chemistry C* **7**, 3945–3951 (2019).

Chapter 4. High-efficiency Quasi-2D Perovskite LEDs using Vapor-deposition methods

4.1. Introduction

New luminescent system based on MHPs with high color purity, low cost, and easy color tunability should be realized to achieve high-quality optoelectronic devices with vivid display.¹ Especially, solution-process PeLEDs are outstanding results so far.²⁻⁶ However, there is limitation of solution process such as fabrication difficulty of large-area devices, narrow material choice, and low reproducibility. Therefore, thermal evaporation has been attention for the replacement of solution process. We already introduced the pros and cons of evaporation technique, and some methods for the perovskite thermal deposition. Here, we briefly show the research progress of thermal deposited PeLEDs.

The first thermal-evaporated PeLEDs was based on the inorganic perovskite because of easy tuning of rate control. They used the co-evaporation of CsBr and PbBr₂, and the maximum EQE of PeLEDs was 1.55%.⁷ Subsequently, improved paper are reported (EQE_{max} ~ 2.5%) through simple composition optimization with same inorganic perovskite. In 2020, the quasi-2D BA-CsPbBr₃ LED constructed by thermal evaporation with sequential vapor deposition technique (EQE_{max} ~ 5%).⁸ Recently, thermally evaporated PeLED were demonstrated with a large-area devices (~40.2 cm²) and a high performance EQE of 7.1%.⁹ Especially, very small EQE loss when they made large-area device compare with solution-processed ones. Further, efficient blue LED with thermal deposition is also reported. They used the CsEuBr₃ as an emitter for blue PeLEDs, and even efficient PeLEDs (EQE_{max} ~6.5%).¹⁰ Thermal evaporation is already chosen for OLED because of lots of advantage for

commercialization of display industry. Though, the device performance of thermal evaporated PeLED is very poor comparing with the state-of-the-art solution-processed perovskites, the trend is increasing, even there are very few researchers have been focus on thermally evaporated PeLEDs. In this thesis, we made quasi-2d perovskite with BnABr co-deposition for the first time (**Figure 4-1**). Especially, I could make CsPbBr₃ films with single-source vapor-deposition methods by making CsPbBr₃ powder for the single-source vapor-deposition, and then I control the chemical stoichiometric ratio for the efficient luminance characteristics. Moreover, co-deposited quasi-2D structure are introduced for the vapor deposited PeLEDs. We demonstrate the bright (>1,000 cd m⁻²) and high reproducible PeLEDs. This work shows the possibility of structure modification of perovskite with vapor-deposition methods.

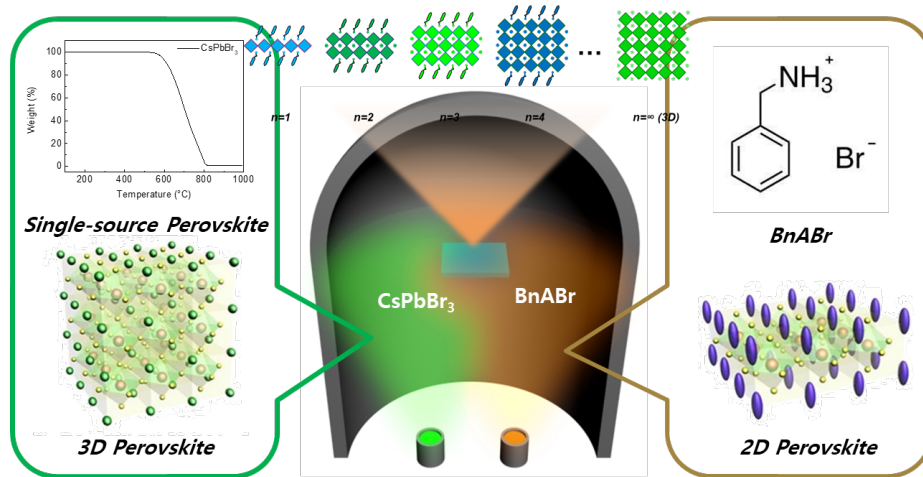


Figure 4-1. Schematic overview of single-source 3D perovskite with BnABr co-deposition

4.2. Materials and Experiments

Materials.

All reagents were used as received without any purification: 1,3,5-Tris(1-phenyl-1H-benzimidazol-2-yl)benzene (TPBI) was purchased from OSM. Cesium bromide (CsBr), Benzyl ammonium bromide (BnABr, 99.99%), lithium fluoride (LiF, 99.99% trace metal basis), dimethyl sulfoxide (DMSO, 99.8%, anhydrous) were purchased from Sigma-Aldrich.

Fabrication of $\text{Cs}_x\text{BnA}_y\text{PbBr}_3$ films.

The sources were directed upward respect to the bottom of the evaporator. The distance between substrate holder and evaporation source was approximately 50 cm. Four quartz crystal microbalance (QCM) sensors were used: three monitoring the deposition rate of each evaporation source and a third one close to the substrate holder monitoring the total deposition rate (we only used three sensor in this thesis). The materials were sublimed at temperatures ranging from 140 to 500°C approximately. Inorganic CsPbBr_3 have higher sublimed temperature, and BnABr have low temperature. Precise rate control was key. Therefore, the evaporation rate was controlled by separate QCM sensors obtaining precisely the deposited thickness. For CsPbBr_3 films, we made different stoichiometric controlled CsPbBr_3 powder (methods of powder would be described in result section). Rate of CsPbBr_3 were 1.0

A/s. For the quasi-2D perovskite, BnABr were co-deposited with different rate control (0.3~to 1.0 A/s)

PeLED Fabrication.

Glass/FTO/GraHIL¹¹/ Cs_xBnA_yPbBr₃ was fabricated as mentioned above. On the perovskite layers, 45 nm of TPBI, 1 nm of LiF, and 100 nm of Al were thermally deposited in sequence in a high-vacuum chamber. Especially, this chamber is different with perovskite deposition chamber. The devices were encapsulated in N₂ atmosphere.

Characterizations of Cs_xBnA_yPbBr₃ films.

The glass/GraHIL/ Cs_xBnA_yPbBr₃ films were encapsulated under N₂ atmosphere for UV/vis, steady-state PL, and time-correlated single photon counting (TCSPC) measurements. UV/vis absorption spectra of the glass/GraHIL/ Cs_xBnA_yPbBr₃ films were obtained using a UV-Vis spectrophotometer (Cary-5000). Steady-state PL spectra were measured using a spectrofluorometer (JASCO FP8500). Xenon arc lamp with continuous-output power of 150 W was used as an excitation source, and the excitation wavelength was 365 nm. The light was incident toward the glass side that is opposite to the Cs_xBnA_yPbBr₃/N₂ interface. To measure PL lifetime, a photon-counting detector (PMA Hybrid 07) and time-correlated single-photon counting

(TCSPC) module (PicoHarp, PicoQuant) were used. Instrument response function (IRF) was ignored because the PL lifetime curves were much longer than the temporal width of the IRF. The excitation power density was $\sim 25 \text{ mW cm}^{-2}$, and the excitation wavelength was fixed at 365 nm.

The X-ray diffraction (XRD) measurement was performed using an X-ray diffractometer (BRUKER MILLER Co., D8-Advance) with Cu K α radiation ($\lambda = 1.54056 \text{ \AA}$). XRD data were gained in the 2θ range of 5° - 40° at room temperature. Top-view and cross-sectional scanning electron microscopy (SEM) images of Si wafer/GraHIL/ $\text{Cs}_x\text{BnA}_y\text{PbBr}_3$ films were measured using a field emission SEM (MERLIN compact, ZEISS) at the Research Institute of Advanced Materials, Seoul National University.

Ultraviolet and X-ray photoelectron spectroscopy (UPS and XPS) spectra of si-wafer/GraHIL/ $\text{Cs}_x\text{BnA}_y\text{PbBr}_3$ films were measured using a photoelectron spectrometer (Kratos Inc., AXIS-Ultra DLD). in collaboration with Korea Basic Science Institute (KBSI).

Characterization of PeLED Devices.

The fabricated devices were encapsulated in N_2 atmosphere and transferred to air for characterization. The current-voltage-luminance characteristics of PeLEDs were

measured by using a source-measurement unit (Keithley 236), a spectroradiometer (Minolta CS-2000), and a control computer as described previous paper.¹²

4.3. Results and Discussion

To the single-source deposition process, a perovskite powder having the structure of ABX_3 was synthesized. Comparative experiments based on organic-inorganic hybrid perovskite ($MAPbBr_3$) and inorganic perovskite ($CsPbBr_3$) was done to find suitable cations for single source deposition process. Firstly, we made the precursor solution of ABX_3 using DMSO as a solvents. Then, addition of HBr to the perovskite precursor solution to cause a crystallization reaction (**Figure 4-2**). It is important to control the reaction rate by adding HBr dropping speed to obtain a uniform size powder. As the amount of HBr addition increased, color changing (from yellow to orange color in **Figure 4-2**) was shown because of crystallization reaction occurs actively. Amount of HBr should be the same volume ratio of precursor solution. After all the reactions are complete, the purification process using ethanol is performed to remove impurities, and then thoroughly dry in a vacuum oven (over 12 hours, usually overnight) to completely blow off the solvent to obtain a perovskite powder having an ABX_3 structure. After fully drying the perovskite powder, physical milling process was done for the fine ABX_3 powder.

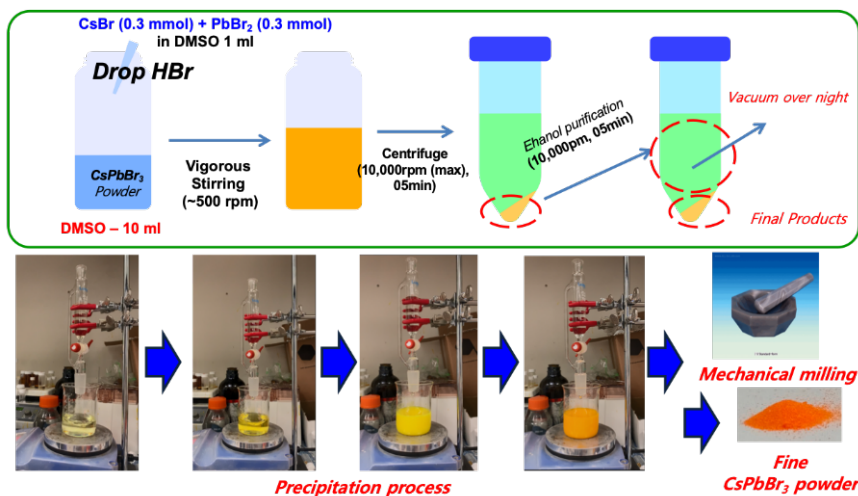


Figure 4-2. CsPbBr₃ powder synthesis for the single-source perovskite films

TGA analysis was performed using two different perovskite powders (CsPbBr₃ & MAPbBr₃) synthesized to determine whether single-source deposition was possible (Figure 4-3). First, it was confirmed that the perovskite powder was well formed by TGA analysis pattern of CsPbBr₃ as reported in the literature.¹³ MAPbBr₃ powder was decomposed into MABr and PbBr₂, but there is no decomposition curve into CsBr and PbBr₂ in CsPbBr₃ powder. This shows the inorganic perovskite, CsPbBr₃, is more strongly bound, suggesting that single-source perovskite deposition is possible.

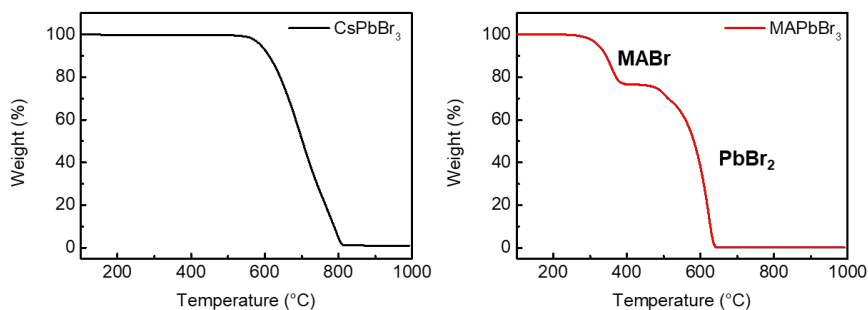


Figure 4-3. TGA Analysis with CsPbBr₃ powder and MAPbBr₃ powder.

In order to improve the low luminous characteristics of the perovskite emission layer, stoichiometric ratio control was introduced. We change the ratio of CsBr and PbBr₂ when producing CsPbBr₃ precursor. TGA analysis with different CsPbBr₃ powder (ratio of CsBr and PbBr₂ was 1.0:1 to 3.0:1) was done to know whether single-source deposition is still possible (**Figure 4-4**).

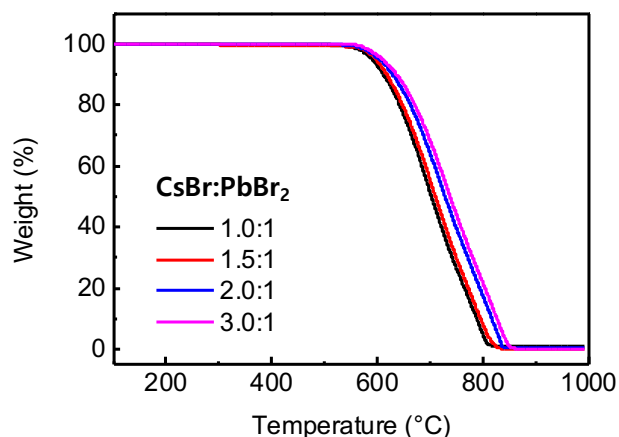


Figure 4-4. TGA Analysis with CsPbBr₃ powder with stoichiometric control.

As the ratio of CsBr increased, it was confirmed that CsPbBr₃ was decomposed at a slightly higher temperature, but it still did not dissociate into two substances like MAPbBr₃ powder. It means that we could do single source deposition through stoichiometry-controlled powder. Metallic Pb in perovskite are the quencher, so exciton recombination is suppressed.⁶ Therefore, we also conducted the X-ray photoemission spectroscopy (XPS) analysis with different stoichiometric CsPbBr₃ films (**Figure 4-5**). As you can see, excess CsBr ratio hinder the formation of metallic Pb peak in XPS, so exciton quenching because of metallic Pb would be decreased with stoichiometric control.

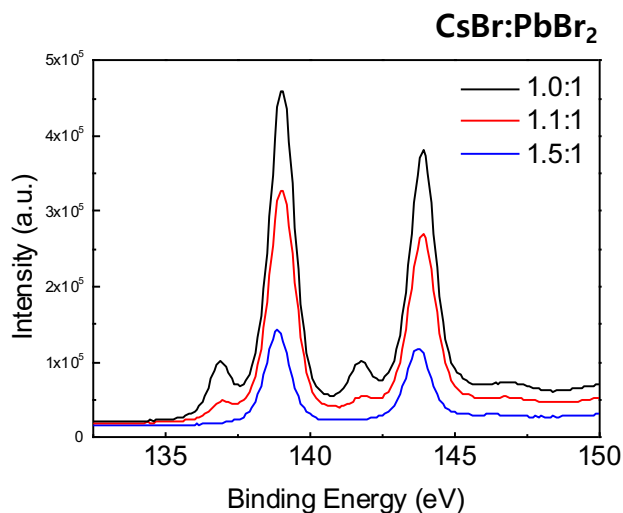


Figure 4-5. XPS Analysis with CsPbBr₃ powder with stoichiometric control.

A single-source thermal deposition perovskite thin film was prepared using the previously synthesized CsPbBr₃ powder, and its opto-physical properties were analyzed to confirm the CsPbBr₃ films is well made (**Figure 4-6**). Steady-state PL and UV-vis spectra are same with previous CsPbBr₃ perovskite films, and XRD data also show the simple cubic structure of CsPbBr₃.

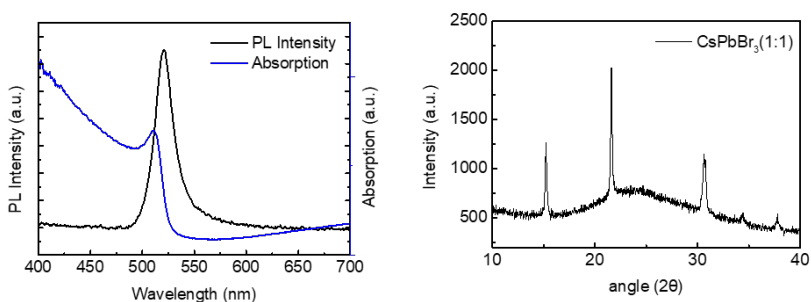


Figure 4-6. Photophysical properties of single-source vapor evaporation CsPbBr₃ film

Steady-state PL characteristics by controlling the stoichiometric control from 1.0:1 to 3.0:1 are analyzed. It was found that the ratio of CsBr to PbBr₂ had the highest emission intensity when 1.5:1, which showed the same trend as the PL

lifetime result. It can be confirmed that they have (Figure 4-7). This is interpreted as the radiative recombination occurs more because of the lower metallic Pb species. Additionally, from the result that the peak position of the normalized PL does not change at all, it can be inferred that the perovskite structure itself does not change and only the luminescence characteristics are improved. It was also confirmed with no change with UV-vis spectra and XRD peak.

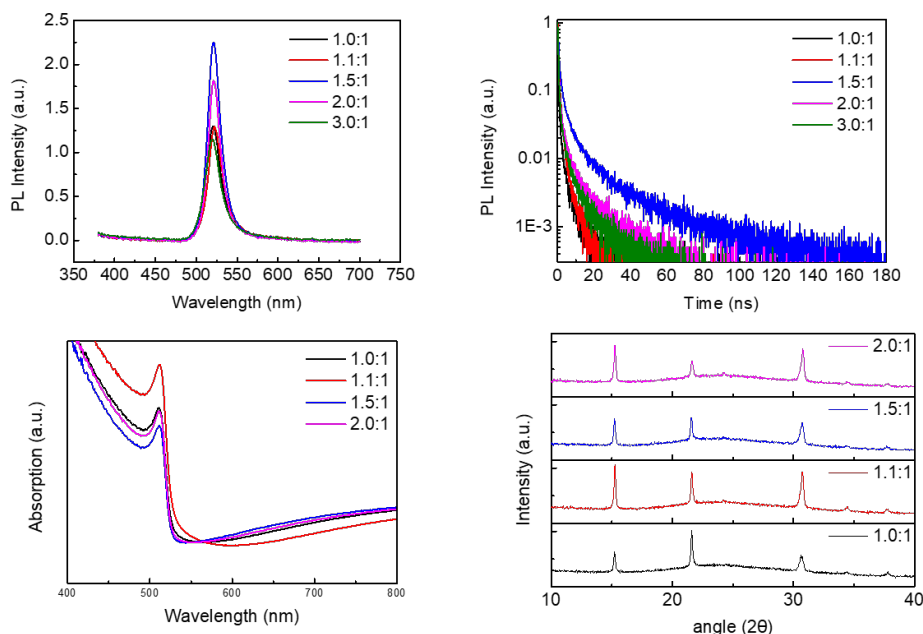


Figure 4-7. Photophysical properties of fine-stoichiometry control vapor evaporation CsPbBr₃ film

Finally, in order to realize the highly luminance polycrystalline perovskite, quasi-2D perovskite was introduced using co-deposition technique. We choose the Benzyl ammonium bromide as a long-alkyl ammonium. Especially, quasi-2d structure have natural quantum-well structure, then energy funneling are occur in their own structure.^{14,15} We precisely control the co-deposition rate and could demonstrate the different n value are formed by thermal deposition (Figure 4-8). Luminescence characteristics are analyzed obtained by co-deposition at various ratios of

CsPbBr₃:BnABr ratio (different n value). First, great improvement of photoluminescence properties according to the BnA co-deposition ratio is shown in **Figure 4-8**. As shown in the figure, as the n=3 films has the best PL intensity, it was also confirmed PL lifetime and picture of films that are under UV-lamp. Dramatic enhancement are showed because of quantum-well structure of quasi-2d structure. Moreover, we could see the n1, n2, n3 peak in the normalized PL curve. It demonstrate that the quasi-2D perovskite is well-formed.

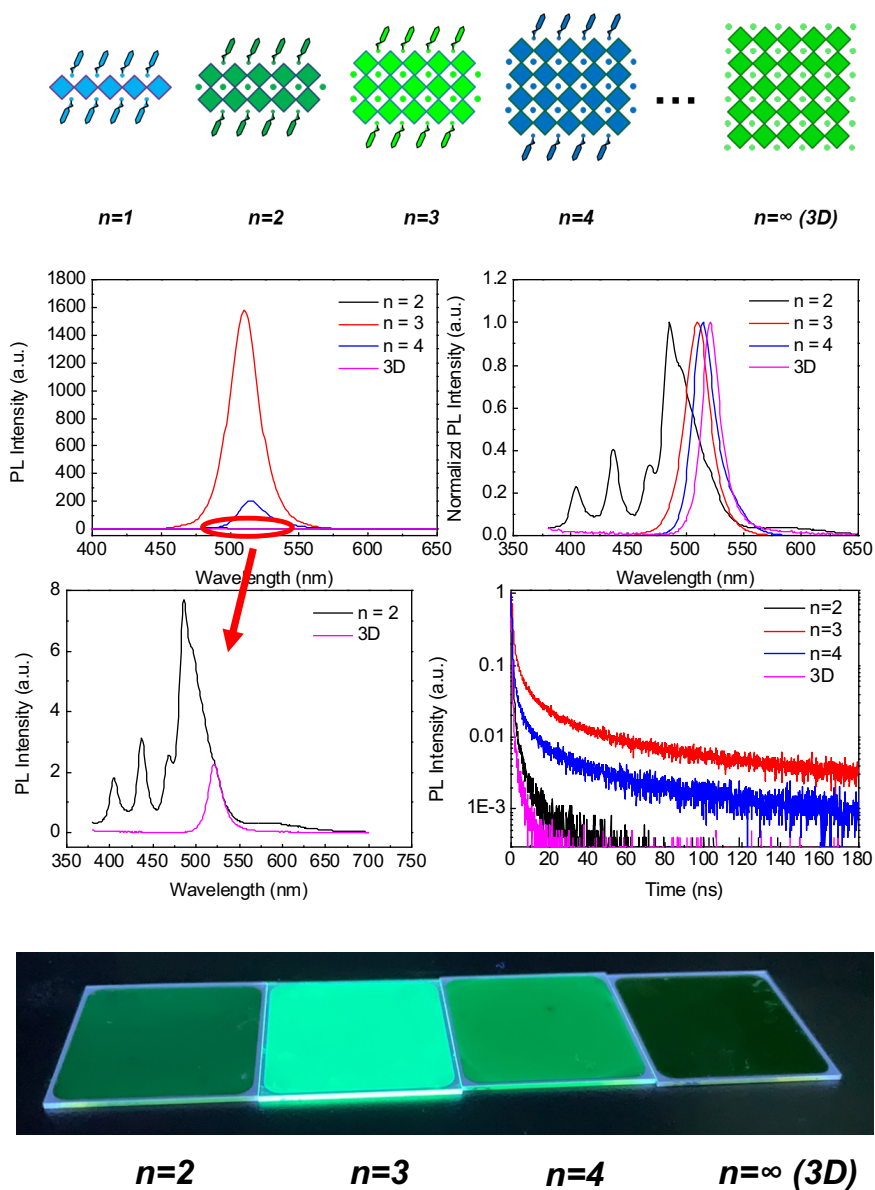


Figure 4-8. Illustration of quasi-2D phase distribution, and steady-state PL and PL Lifetime analysis with Quasi-2D perovskite films, picture of different n value films under UV

Additionally, UV-vis spectra and XRD peak also show the low-dimension perovskite peak (**Figure 4-9**). Low dimension perovskite peak is clearly show with larger BnABr co-deposition ratio. All the low-dimension peak position is same with previous paper.

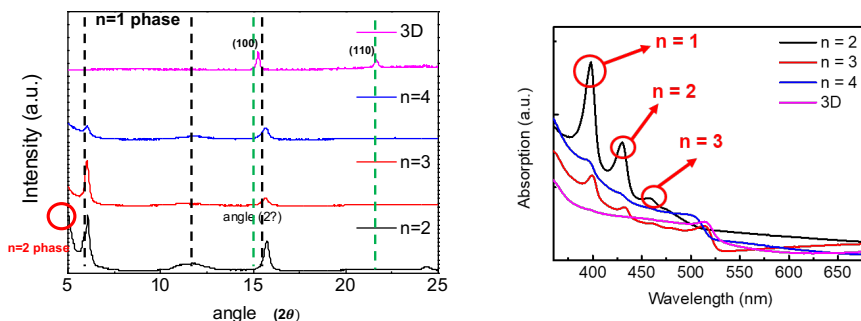


Figure 4-9. 2D characteristics with XRD and UV-vis Absorption spectrum.

SEM analysis was performed to observe the distribution and shape of the actual crystals of the perovskite thin film made by co-deposition (Figure. 4-10).

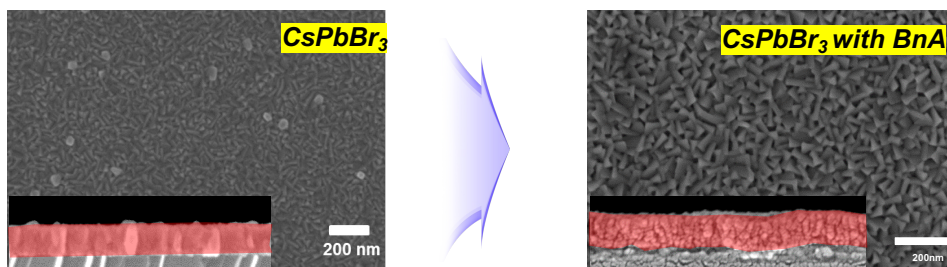


Figure 4-10. SEM image of CsPbBr₃(3D) and CsPbBr₃ with BnABr (Quasi-2D)

It can be confirmed that the aggregation phenomenon, which has been the biggest problem of perovskite using the deposition process so far, has been completely resolved through co-deposition with BnABr, and the crystal size is also very smaller. Also, it can be confirmed that the shell-structured of polycrystalline perovskite is realized, it's very similar with previous data with 2D/3D hybrid structure formation.¹⁶ This may be due to the following reasons. 1) BnABr are bonding with CsPbBr₃ in the crystallization process, prevents the self-assembly of inorganic CsPbBr₃ itself and aggregation. 2) Compared to inorganic CsPbBr₃, which is a polar material. It change the surface energy difference from the surface of the bottom side,

so it is easily adsorbed to the surface to facilitate the formation of crystal nuclei, resulting in higher crystallization density.

We also made the PeLEDs based on these properties to comparing different n value (**Figure 4-11**). Also, PeLEDs based on $n=3$ are excellent device efficiency with maximum brightness (L_{\max}) $> 1,000\text{cd m}^{-2}$ and maximum current efficiency (CE_{\max}) $> 2.0\text{ cd A}^{-1}$. 3D perovskite have no emission, and no diodic characteristics, this comes from the aggregation of the films and high defect density of 3D perovskite films. Histogram of quasi-2D PeLEDs also done (**Figure 4-12**). This demonstration was same tendencies with PL and PL lifetime.

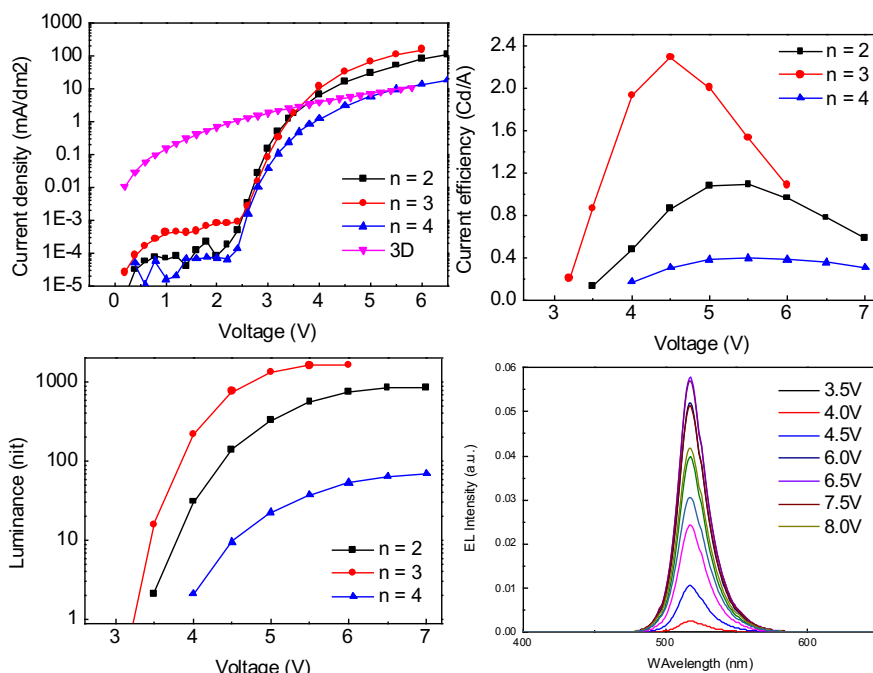


Figure 4-11. J-V-L Characteristics with different n value of vapor-deposition Quasi-2D PeLEDs

Especially, narrow EL spectrum are showed ($\sim 20\text{nm}$). The results are still low performance compare with solution processed quasi-2D PeLEDs, but it's the first quasi-2D PeLEDs by thermal deposition with co-deposition methods. The result

indicates that the BnABr co-deposition are affected the opto-physical properties of perovskite, and the devices are also working well. Therefore, the quasi-2D system could stabilize the crystal structure and passivate the defect states.

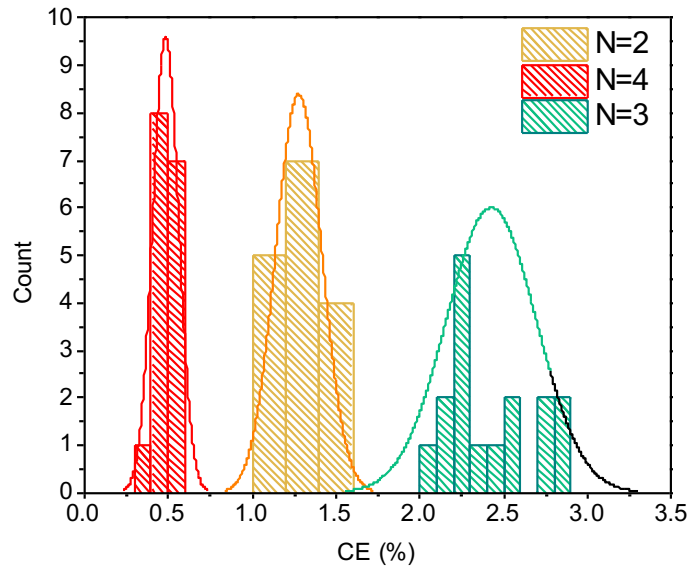


Figure 4-12. Histogram of CE with Quasi-2D PeLEDs

4.4. Conclusion

In conclusion, vapor-deposition method is introduced. In these days, most of researcher have focused on the solution-processed perovskite optoelectronics because of easy-fabrication characteristics. However, vapor-deposition methods are needed for the commercializing of perovskite as an emitter. Therefore, I introduce the physical vapor methods for PeLEDs. Especially, I could make CsPbBr₃ films with single-source vapor-deposition methods by making CsPbBr₃ powder for the single-source vapor-deposition, and then I control the chemical stoichiometric ratio for the efficient luminance characteristics. Moreover, quasi-2D structure are firstly introduced for the vapor-deposited PeLEDs. I could see the energy funneling effect by structure modification and demonstrate the bright ($>1,000 \text{ cd m}^{-2}$) PeLEDs. This work shows the possibility of structure modification of perovskite with vapor-deposition methods.

4.5. Bibliography

1. Quan, L. N. *et al.* Perovskites for Next-Generation Optical Sources. *Chemical Reviews* **119**, 7444–7477 (2019).
2. Kim, Y.-H. *et al.* Comprehensive defect suppression in perovskite nanocrystals for high-efficiency light-emitting diodes. *Nature Photonics* **15**, 148–155 (2021).
3. Zhao, B. *et al.* High-efficiency perovskite-polymer bulk heterostructure light-emitting diodes. *Nature Photonics* **12**, 783–789 (2018).
4. Xiao, Z. *et al.* Efficient perovskite light-emitting diodes featuring nanometre-sized crystallites. *nature.com*.
5. Lin, K. *et al.* Perovskite light-emitting diodes with external quantum efficiency exceeding 20 per cent. *Nature* **562**, 245–248 (2018).
6. Cho, H. *et al.* Overcoming the electroluminescence efficiency limitations of perovskite light-emitting diodes. *Science (1979)* **350**, 1222–1225 (2015).
7. Hu, Y. *et al.* Vacuum-evaporated all-inorganic cesium lead bromine perovskites for high-performance light-emitting diodes. *pubs.rsc.org*.
8. Lian, X. *et al.* Light emitting diodes based on inorganic composite halide perovskites. *Wiley Online Library* **29**, (2018).
9. Fu, Y. *et al.* Scalable All-Evaporation Fabrication of Efficient Light-Emitting Diodes with Hybrid 2D–3D Perovskite Nanostructures. *Wiley Online Library* **30**, (2002).
10. Luo, J. *et al.* Efficient blue light emitting diodes based on europium halide perovskites. *Wiley Online Library* **33**, (2021).
11. Kim, Y.-H. *et al.* Multicolored Organic/Inorganic Hybrid Perovskite Light-

- Emitting Diodes. *Advanced Materials* **27**, 1248–1254 (2015).
12. Jeong, S.-H. *et al.* Characterizing the Efficiency of Perovskite Solar Cells and Light-Emitting Diodes. *Joule* **4**, 1206–1235 (2020).
 13. Cho, H. *et al.* High-Efficiency Solution-Processed Inorganic Metal Halide Perovskite Light-Emitting Diodes. *Advanced Materials* **29**, (2017).
 14. Yuan, M. *et al.* Perovskite energy funnels for efficient light-emitting diodes. *Nature Nanotechnology* **11**, 872–879 (2016).
 15. Byun, J. *et al.* Efficient Visible Quasi-2D Perovskite Light-Emitting Diodes. *Advanced Materials* **28**, 7515–7520 (2016).
 16. Kim, H. *et al.* Proton-transfer-induced 3D/2D hybrid perovskites suppress ion migration and reduce luminance overshoot. *Nature Communications* **11**, 3378 (2020).

Chapter 5. Summary

Metal halide perovskite (MHP) have outstanding optoelectronic properties: 1) easy color tuning, 2) good photoluminescence, 3) narrow emission spectrum (small full width at half-maximum length), and 4) balanced charge carrier mobility. Then, the materials have been studied a lot for the display application. Various strategies are introduced for the achieving high performance perovskite light-emitting-diodes (PeLEDs). Then, outstanding results have been reported so far, but some area still need to overcome the limitation of PeLEDs. In this thesis, we develop highly efficient and stable PeLEDs by structure modulation. These results are almost same with conventional commercialized LED devices. Three main idea is crystal structure engineering: 1) sulfur-cooperative additive engineering, 2) A-site cation modification, and 3) introducing longer organic alkyl ammonium using thermal evaporation for dimension control of perovskite.

In the first chapter, brief introduction of what is perovskite materials and then, the meaning of structure modulation in perovskite fields. Also, basic introduction of thermal deposition technique in PeLEDs. Lastly, overview of research idea are shown. **In The second chapter**, 1,8-octanedithiol (ODT) are introduced as an additive for suppression of exciton loss in single cation perovskite (MAPbBr₃). Especially, the ODT dominantly distributed at the interface between emitting layer (MAPbBr₃) and bottom hole injection layer. Also, ODT distributed at the grain boundary because of bonding with uncoordinated Pb²⁺. This suppression of exciton loss make improvement of PeLEDs' efficiency and stability, and these are best performance with single-cation PeLEDs (EQE: 14.2% and T₅₀: 139 min). **In the**

third chapter, we introduce the quadruple cation perovskite structure for defect passivation of 3D polycrystalline perovskite. Recently, mixed-cation system have been reported for making PeLEDs that have highly efficient characteristics, but these have not been realized high luminance, high efficiency and long lifetime at the same time. Polycrystalline 3D perovskites have excellent charge transport properties intrinsically, but they have lots of defect states in their crystal structure. In this thesis, we invent the ideal mixed cation system using Guanidium (GA) cooperation into A-site cation in crystal structure. Especially, we also using MA cooperation into A-site for maximize the advantages of GA cation. We could incooperate the GA into FA-site 20 molar ratio, and could demonstrate efficient, bright, and stable green PeLEDs that have maximum brightness of $\sim 470,000 \text{ cd m}^{-2}$, maximum current efficiency of 150 cd A^{-1} (external quantum efficiency of 28.94%), and very long estimated half-lifetime of $>14\text{h}$ at $100,00 \text{ cd m}^{-2}$. We show that quadruple cation system can effectively passivate the high defect nature of polycrystalline 3D perovskite, and thereby realize strong charge confinement and greatly reduced trap density while maintaining the good charge transport properties of 3D perovskites. **In the fourth chapter**, new project (thermal evaporation) is introduced. Solution-process are good methods in lab-scale experiments. However, new methods are needed for the commercializing of perovskite as an emitter. Therefore, we introduce the physical vapor methods for PeLEDs. Especially, we could make CsPbBr_3 films with single-source vapor-deposition methods by making CsPbBr_3 powder for the single-source vapor-deposition, and then we control the chemical stoichiometric ratio for the efficient luminance characteristics. Moreover, quasi-2D structure are firstly introduced with co-deposition of 3D part (CsPbBr_3) and BnABr simultaneously. We could see the strong luminance characteristics because of energy

funneling effect and quantum-well structure formation. Finally, we could demonstrate the bright ($>1,000 \text{ cd m}^{-2}$) PeLEDs. This work shows the possibility of structure modification of perovskite with vapor-deposition methods. With the presented findings, a better understanding of the perovskite structure modulation, and could be the cornerstone of commercialization of PeLEDs.

Abstract in Korean

금속 할로겐화 페로브스카이트는 아래와 같은 분야에 활용 가능 한 물질로 최근에 많은 각광을 받고 있습니다 (태양 전지, 발광 다이오드, 레이저, 트랜지스터, 그리고 기억 장치 등). 특히, 하이브리드 페로브스카이트는 i) 쉬운 색상 조절, ii) 우수한 광발광, iii) 좁은 방출 스펙트럼 및 균형 잡힌 전하 캐리어 이동성과 같은 발광체 활용에 우수한 특성을 가지고 있습니다. 이러한 장점을 바탕으로 연구원들은 2012년 최초의 실온 페로브스카이트 발광 다이오드 이후 구조적 접근, 결정화 조절 방법, 차원 조절과 같은 많은 전략이 도입 되어 연구가 진행되어 왔습니다. 그러나 효율적인 대면적 페로브스카이트 발광 다이오드의 개발은 결정 구조 불안정성의 한계와 용액공정의 한계로 인해 아직 개발이 미진한 실정입니다.

본 학위 논문에서는 결정 구조 변화를 통해 고효율 및 안정적인 페로브스카이트 발광 다이오드를 개발에 관한 연구를 진행 하였습니다. 특히, 이러한 결과는 기존에 사용화 된 유기 발광 다이오드 와 양자점을 이용한 발광 다이오드와 같은 상용화된 발광 다이오드와 비슷한 수준의 효율을 자랑 합니다. 본 학위논문의 주요 접근 방식을 크게 세가지로 첨가제 도입, 양이온 치환을 통한 이상적인 양이온 구조 도입, 증착 공정에서의 차원 조절 연구 입니다.

첫 번째 장에서는 간단하게 페로브스카 라는 물질에 대한 간단한 소개와 함께, 페로브스카이트 결정 구조 및 페로브스카이트 발광

다이오드에서 활용 되는 증착 공정에 대해 간단 하게 설명 하고자 합니다.

두 번째 장에서는 첨가제를 단일 양이온 페로브스카이트 물질에 적용 하는 연구 입니다. 페로브스카이트의 결함 제어 및 여기자 손실 억제는 페로브스카이트 발광 다이오드의 특성에 크게 영향을 끼칩니다. 여기에서는 1,8-octanedithiol 라는 첨가제를 활용하여 페로브스카이트 층과 하부 정공 주입 층 사이의 계면에서 결함을 막고, 결정 구조 내부의 결함도 제어 할 수 있습니다.

세 번째 장에서는 3차원 다결정 페로브스카이트의 결함 제어를 위한 4중 양이온 페로브스카이트 구조를 소개합니다. 최근 고효율 특성을 갖는 페로브스카이트 발광 다이오드에 대한 논문이 많이 보고 되고 있지만, 고휘도, 고효율, 장수명을 동시에 구현 하는 논문은 아직 보고되지 못하였습니다. 다결정 3차원 페로브스카이트는 본질적으로 우수한 전하 수송 특성을 가지고 있습니다. 그러나 높은 결함 밀도로 인해 높은 발광 효율을 얻기에는 적합하지 않는 단점이 있습니다. 한편, 페로브스카이트 나노결정은 강한 캐리어 구속과 낮은 결함 밀도를 가지고 있지만, 절연 리간드로 인해 전하 수송이 좋지 않아 밝기가 낮고 작동 수명이 낮은 단점이 있습니다. 여기에서 우리는 결정 구조의 A-사이트 양이온으로 Guanidium(GA)를 치환 하여 결함이 없는 4중 페로브스카이트 결정 구조를 보고 합니다. 특히, 우리는 $\sim 470,000\text{cd m}^{-2}$ 의 최대 밝기, 150cd A^{-1} 의 최대 전류 효율 (28.94%의 외부 양자 효율) 및 $100,000\text{cd m}^{-2}$ 에서 14 시간 이상의 매우 긴 수명을 가지는 안정적인 녹색

페로브스카이트 발광 다이오드를 구현 하였습니다.

네번째 장에서는 페로브스카이트 발광 다이오드 상업화에 큰 걸림돌인 대면적화의 어려움과 낮은 재현율을 극복하기 위해 증착 공정을 통한 페로브스카이트 발광 다이오드 구현에 관한 연구를 진행 하였습니다. 특히, 단일 소스를 활용한 증착 무기 CsPbBr_3 페로브스카이트를 구현 하였습니다. 추가적으로, 효율 적인 광발광 특성을 위해 화학양론 조성 조절을 도입 하였습니다. 또한, 공증착 방법을 통한 Quasi-2D 페로브스카이트 구조를 도입 하는 연구를 진행 하였습니다. 이를 통해 양자 우물 효과를 통한 효율적인 광발광 특성 향상을 관찰 하였으며, 이를 활용한 소자 제작을 통해 밝은 ($>1,000\text{cd m}^{-2}$) 페로브스카이트 발광 다이오드를 구현 할 수 있었습니다. 본 학위 논문에서 제시된 연구 결과를 통해 페로브스카이트 구조 변화에 대한 이해와 페로브스카이트 발광 다이오드 기술 상용화의 초석이 될 수 있을 것으로 기대 합니다.